Interactive comment on "Mesospheric gravity wave activity estimated via airglow imagery, multistatic meteor radar, and SABER data taken during the SIMONe–2018 campaign" by Fabio Vargas et al.
Anonymous Referee #1
Received and published: 5 October 2020

This manuscript presents a fairly detailed investigation of gravity waves observed in airglow image data obtained during an observation campaign in November 2018, from Northern Germany. It is well-written and provides a good assessment of the effects of GW on the mesosphere, even if it is during a limited period of time. However, the authors should address the following would comments:

- We thank you for raising these important comments and suggestions. We address your comments the better we can.

- It is a little bit surprising that there are no waves with intrinsic period <20 min. Most of the waves should be propagating against the wind, therefore their intrinsic phase speed should be larger than the observed one, and their intrinsic period should be smaller than their observed one.

- In figure 5f, the reviewer can see that there are waves traveling against the wind, waves traveling nearly perpendicular to the wind, and in few cases, waves propagating to the same wind direction. Although there are a few waves traveling to the same wind direction because their larger phase speed, these waves do not transport significant momentum flux, as presented in figure 5a showing large momentum flux waves moving against the wind.
- We did not detect waves with periods <20 min, although they must be present certainly. Due to the filter wheel cycle time, a given airglow emission is sampled every 10 min, which allows only the detection of waves having periods >20 due to the long sampling period of 10 min each image is acquired.

- lines 255-271: It is complicated to compare the results with Li et al., 2011, because of the time resolution (~10 min) which does not allow for detecting most short-wavelength, short-period waves. As also noticed in the manuscript, this campaign covered only a few days, while Li et al. results represent the whole year. Same problems with Li, 2011.

- We did the comparison because the paper utilizes the same autodetection technique. we focus on the results of Li et al which are comparable to the wave scales we have detected. A stronger correspondence between the results is found in the longer horizontal wavelength range (100 kilometers or longer), which are associated to convective sources far away from the observation site. In this way, we can verify that our findings are in agreement with those of Li at al. (2011), even in the case we do not detect the shorter period waves, shorter horizontal scale waves.

- lines 284-285: These mean values are very small, especially considering the error. What does -0.36+/-1.51 mean? - 0.36+1.51=1.15, so the MF is carried in the other direction? Or you are sure about the wave direction of propagation, and so the minimum possible value is 0? I am not sure how it is possible to measure such small MF values giving the uncertainties in the measurements.

- The summary box in Fig. 5 shows the MF mean and MF standard deviation of the sample, not the error in the MF determination. Notes that the error in momentum flux must take into consideration the errors in all the wave parameters determined by our auto detection method for wave event (see Vargas, 2019). As we showed and discussed in the manuscript, most of the waves carry small momentum flux, and this fact reflects on the mean, which is very small. The standard deviation shows more or less the spread in the data, that is, the distribution of waves going to one side against those going to the opposite side.

- line 286: The total value is very misleading and cannot be used for any future comparisons. With the analysis method used in this paper, GWs are measured for each image, therefore the more images, the larger the total MF. If the imager cycle was 1 min instead of 10 min, the total MF would be 10x larger because 10x more waves parameters would have been measured! An average MF value for each wave and its duration could be more useful to assess its impact. The statistical results (11% of the waves responsible for carrying 50% of the MF...) are still relevant but the authors have to be very careful when giving the "total" MF. -

- I agree the total MF value means nothing and will cause confusion. To give a meaningful estimation of the total momentum flux, we should have found the number of independent waves (see our reply to your next comment). We have removed the total MF from the paper.

The number of waves detected (362) is also controversial. There were NOT 362 separate GWs propagating over the observation site during these 4 nights! There were 362 wave measurements, which is different. Some of the waves probably lasted for hours and their parameters were measured several times. Of course, these parameters can evolve depending on the forcing and the background atmosphere conditions, but there were still the same GWs coming from the same sources

- The waves are not necessarily independent. We have defined as a gravity wave event the output of the cross-spectrum of two time-difference images when the special peak is larger than 10% of the total energy of the spectrum. two time-difference images are generated from three light frames of the airglow. Thus, if a wave is detected in a given set of three light images, it is considered an independent wave detection. If, in the next set, another wave detection is made, the only way to tell the two events correspond to the same gravity wave is by comparing their wave parameters, which vary among image sets. Now, the momentum flux of a wave varies as it goes through the field of view as well. Thus, considering the mean MF of all the waves detected during the campaign would be the same if we cluster the corresponding wave events into a distinct wave, average the momentum flux for that specific wave for the duration of the event over the airglow images where it shows up, and then average over all the distinct wave events found. This less efficient and more laborious though. We have a clustering algorithm that does that work for us, but still, we choose not to do it in the present manuscript.
- As we rely on a set of three images at the time from where we obtain two time-difference images, and finally the cross spectra from the 2DFFT of the time difference images. So, the time span of each set is about 30 min, and most of waves would have completely disappeared the imager FOV within that time span because the duration of a gravity wave is short based on our experience. This way, it would be more likely that each detection corresponds to an independent wave detection.

The GWs were observed in 4 different airglow layers, at 4 different altitudes. Could you give more information about that? Which waves were observed simultaneously? It would also be interesting to see the difference in MF between the airglow layers.

- The momentum flux of waves in different layers can be given and we have estimated it separately, but because the detections in an individual layer were not too many, we showed the results together. We have provided separated plots analogous to figure 5 as supplementary material where the reviewer can see the wave detections over time in individual layers.

The MF divergence would be very interesting, as well. - You should mention ducted waves. Even if the waves presented in this paper are unlikely to be ducted because of the minimum intrinsic periods, these waves exist but do not carry any vertical MF, so they would bias your results. Again, a comparison between the different airglow layers would help

- Estimating the momentum flux divergence between two layers is possible and we have done that in Vargas et al, 2015, http://dx.doi.org/10.1016/j.asr.2015.07.040. The simultaneous identification of a wave in two layers is more demanding, and we do that for specific, individual cases. Instead of that, here we have estimated the flux divergence from our model (Vargas et al, 2007, JOURNAL OF GEOPHYSICAL RESEARCH, VOL. 112, D14102, doi:10.1029/2006JD007642, 2007) based on the distribution of periods and wavelengths of the observed waves. In this paper, we have done that as if the wave amplitude was measured in the OH and O(1S) layers simultaneously, with no change in amplitude detected (saturated waves).

- It is probably beyond the scope of this paper, but given the small number of nights, looking for sources (tropospheric weather, convection, fronts...) would be interesting.

- We did not address the sources of the waves in this paper but will do it in a follow up publication exploring the sources of primary and secondary waves based on the possibility of secondary wave generation in the range of 30-40 km as suggested by lidar temperature data.

Minor comments:
line 12: can you add the number of nights/hours of observation? It would give a better idea of the importance of the MF values.

- The number of hours per night can be seen an estimated from figure 1 keograms. We have estimated that and added to the text in line 10 (four nights, 45 hours nighttime observations).

line 26: remove "successfully"

- We have removed that.

line 93: long-period variations Section 2.2: what are the vertical and temporal resolutions of the radar system?

- The MSMR data was processed with vertical resolution of 1 km and temporal resolution of 30 min for the total wind field (Fig2a). The fluctuations (Fig2b) were calculated by subtracting the total wind field from a heavily averaged wind with 4-km vertical resolution and 4-hours temporal resolution over 400 km FOV of the MSMR system.

line 137: FWHM

- We have corrected that.

line 175: "duration" instead of "length"

- We have corrected that.

line 177: The MF equation is proportional to Lz/Lx, so it is not that surprising that large horizontal wavelength waves carry less MF. It is more surprising that large vertical wavelength waves carry less MF, though.

- From Vargas et al. (2007), we see that the momentum flux (Eq. 15) is given by $F_M/\rho_u = -\frac{1}{2}\frac{\omega^2 g^2 m}{N^4 k}(\frac{I'/I_0}{CF_I})^2$, and other variables like the cancelation factor (vertical wavelength dependent) and the wave amplitude also are taken into account. Observe that FM has a square dependency on these variables as well as the wave frequency. All in all, because MF is multidimensional in the wave parameter variables and CF, there is no easy way to visualize it in a plot. Maybe would be optimum to show layers where two FM parameters vary while the others are kept constant.

line 191: You must have done your filtering wrong if the cutoff was 5 hours and you still see that many peaks, especially the ones around 6, 8, and 12 hours! The peak at 8.9 hr is pretty close to the peak at 8 hr. You have to give the resolution of the spectra, otherwise this is not very convincing.

- We have not explained correctly the way the wind fluctuations were calculated (it is corrected now in the manuscript). To obtain the wave fluctuations (Fig2b), we first calculate 4-hours, 4-km temporal and spatial windows to average the wind over 400km field of view. then we subtract the result from the total wind field. The total wind field was calculated using much smaller temporal and spatial windows, that is, 30 min and 1 km, respectively. Because that, the resulting fluctuations still keep some of the energy of larger periods waves as can be seen in the spectrum.
- Although we are reducing the effects of tides and waves with periods larger than 4 hours using: (a) temporal filter of 4 hours, (b) altitude filter of 4 kms, and (c) the inherent horizontal filter of about 400 km or so, we can see that signature of 8 hours with large vertical wavelengths and very large horizontal wavelengths are still visible.
- Looking to the spectrum alone we cannot tell apart tides to gravity waves. However, we can identify larger periods gravity waves in the airglow because their horizontal wavelength is ~1000 km whereas the tidal components have much larger horizontal scales. This way, the ~1000 km, 8 hours waves can be seen in the airglow keograms as the tilted brightness structures as those in Fig. 8b.

line 204: The keograms could be improved by flat fielding the images first. Not sure if this had been done, but it would improve the signal at the zenith compared to the edges. Figure 8a bottom is misleading. It looks like the wave tilt (which is related to the direction of propagation and phase speed) corresponds to the decrease in meridional wind intensity. Not sure how to avoid that. You should add the directions of propagation in Table 3.

- We perform all the pre steps, flat fielding included, before calculating the 2DFFT of the keograms. By simulating a 3D gravity wave perturbing the airglow and using the gravity wave polarization relations from the linear theory, we would be able to confirm that the airglow intensity increases with the decreasing of the meridional wind.

line 221: What is the error on the horizontal wavelength measurements?

- The uncertainty in the horizontal direction can be determined from the horizontal wavenumber spectrum where the spread of the wavenumber energy that leaks to adjacent wavenumbers. From our calculations in Vargas 2019, we have estimated more or less 10% uncertainty (included in the text now) in the horizontal wavelength, that is, ~130 km for the wave seen on Nov. 3-4.

line 235: 8 hours, could be a tidal component.

- As pointed out above, the large-scale wave of Nov 6-7 does not correspond to a tidal component since the horizontal wave structure can be fully seen in the keogram of Fig.8b.

line 293-294: The last sentence is enigmatic. If these larger amplitude waves are only seen in the O2 emission but not below (OH, Na) or above (OI), it is quite puzzling.

- The fact that large amplitude waves are seeing in the O2 layer is surprising given the layers overlapping structures. This must be investigated separately. At this point, we don't have a good explanation. However, the O2 has the narrower estimated FWHM for the campaign, and that would allow shorter vertical scale waves to be seen in the O2 images, and consequently larger momentum flux waves would be measured there (see lines 311 -313).
- We have added the following to that sentence: “It is not clear why the enhanced waves are seen most in the O2 emission once the layer’s peaks nearly overlap, but this could be related to the fact that the O2 VER has the smallest FWHM (see Table 2). These shorter λz waves would be seen in images of the O2 emission primarily, and their momentum flux would be larger for it increases as λz decreases (see Fig. 5i)”..

Lines 363-365: Can you rephrase this sentence? It is not very clear.

- We have removed the referred sentence because it was too speculative.

Line 378: The links are missing!

We have fixed that.

Figure 4: (d) Calculated volume emission rates...

We have fixed that.

Figure 7: Can you add a detection threshold?

- We have fixed that. We have added a horizontal line as a reference for the horizontal threshold.

The comparisons with previous publications are lacking some relevant studies: eg, Bossert et al., 2015, for MF of long period waves, Cao and Liu, 2016, for the impact of large vs small MF GWs, and even on the same topic Hertzog at al., 2012, Plougoven et al., 2013, or Wright et al., 2013. The last 3 describing stratospheric measurements, though. The comparisons with Li, 2011, and Li et al., 2011, are not very relevant except because they used a similar analysis method.

- We explained earlier and offered other reasons of why we did compare our results with those of Li et al. (2011) and Li, 2011.
- We have looked into the suggested references and have decided to use that of Cao and Liu, 2015 and Bossert et al. (2015) to compare with our results. We appreciate the suggestions.

Interactive comment on “Mesospheric gravity wave activity estimated via airglow imagery, multistatic meteor radar, and SABER data taken during the SIMONe–2018 campaign” by Fabio Vargas et al.
Anonymous Referee #2
Received and published: 15 October 2020
This manuscript deals with gravity waves detected using an airglow imager and dis- cusses their effect on the background wind, combining collocating meteor radar net- work data and satellite data as background information. Their effort to make full use of the obtained data during the limited campaign period is much appreciated: expanding their analyses to waves with horizontal scales larger than the field of view of the imager. However, the overall analysis methods often lack detailed explanation and hard to follow, and some part of them even seem inadequately done. The authors are advised to revise the manuscript substantially by addressing the following comments.

- We cannot thank enough the reviewer for taking his/her time to read our manuscript and bring up important comments and suggestions to improve it.
- We recognize we need to expand the description of the data analysis to make it clear for the readers. Also, we believe the keogram spectral analysis would be understandable as we wrote, but it is obvious we need to specify it in more detail in the manuscript.

Major comments:
The sequence interval of the imager observation is 10 min, and the exposure time is mostly 2 min. This means that possible aliasing should be taken into account in the analyses although it is not described in the manuscript. Because of the 2 min exposure, any structure with a period shorter than 4 min will be smoothed out and not be resolved, but those with a period between 4-20 min can easily alias into slower period motions, and significantly affect the results.

- We believe that, because every image of a given airglow layer is taken at 10 minutes pace (the imager filter wheel cycle), we are only able to resolve waves with 20 minutes or longer. However, we believe the aliasing is minimal in this case because the small-scale wave structures (horizontal wavelength less than 725 km) seen in the airglow images are sharp (no smudging).

In detecting wave structures from wind data, a high-pass filter with a cut-off of 5 hr is used. However, the detected wave periods are around 4 and 8 hr, which are close to or longer than the cut-off. The wave amplitudes and also phase structures will be largely affected. Even a spectral analysis is done using the filtered wind, and fluctuation components with periods longer than 4 hr are discussed (Fig 7), leading to the subsequent analyses of those components based on the filtered wind as shown in Figures 8 and 10. Although the authors mention these peaks as ‘leakage’ (line 190), I am afraid that such data treatment is not acceptable at all. What the authors can remove before the spectral analysis in the present case would be only the background wind (mean wind) and trend. Since the imager data is unfiltered, wind values should be treated in a similar manner in comparison.
The details of 2D spectral analysis method shown in Fig 9 are not clear. The keograms shown in Figure 8 are thought to be used, of course, but how is the calculation done? The borders of the keograms can significantly affect the results if miss handled. Isn’t there a possibility that the evening twilight seen around 5 pm affects the results? In other words, what kind of spectral window is applied in the analysis?

- We should not have referred to that as “filtering” because reader will think it as a digital filter operation. Here is how we did it: The total wind field was obtained by processing the raw meteor radar data using a 30-min, 1 km window. To calculate the wind fluctuations, the raw meteor radar data was processed using 4-hours, 4-km averaging windows. Then result was than subtracted from the total wind field resulting in the wind fluctuations associated with gravity waves. We have corrected this in the paper to make it clear for the reader what has been actually done to obtain the wind fluctuations.
- We believe the spectral analysis of the wind fluctuations is not faulty. We did not explain correctly how the wind fluctuations were calculated, but this issue is fixed now. Figure 7 shows indeed the relevant wave amplitudes during the campaign, even though we could not suppress completely the tidal modes. A

significance threshold line (99% confidence) has been added to the plot in figure 7 to show the relevant wave amplitudes and periods.

- We have addressed the issue with the filtering of the horizontal wind for the wind fluctuations. The filtered wind is used to compare with the large-scale waves in the airglow keograms. For correcting the wave period Doppler Shift, we use the total wind at the moment of wave detection, not the filtered wind nor the fluctuations.

Minor comments: Abstract

Line 1 'large and small'

- We have changed that.

Not quantitative. More specific description is wanted. The same comments apply to the other 'small' and 'large' in the manuscript.

- We have provided a quantitative estimation of what large and small horizontal scales mean in this paper (line 130-135).
- The small-scale events refer to waves with horizontal wavelength <725 km, while large-scale events are considered here as having horizontal wavelength >725 km. The 725 km range corresponds to the diagonal line across the field of view of an image mapped into a 512x512 km^2 grid. This way, a 725 km wave would still be fully seen within the image frame (on crest, one trough).

Line 6 'flux divergence estimations'

Momentum flux is estimated, but the divergence does not seem estimated, instead MF is just assumed to be deposited around the mesopause.

- We have calculated the momentum flux of each wave detected in airglow during the four nights of the campaign because the auto-detection method outputs all the wave parameters necessary for the MF calculation. Thus, the momentum flux was calculated for each wave individually. However, the flux divergence was estimated from our simulations carried out in Vargas at al. 2007. The divergence estimations assume the waves are saturated, meaning that the wave amplitude doesn't change between two airglow layers. The assumption that the majority of waves are saturated is based on lidar measurements perform over Maui and SOR Observatory in New Mexico. In our reply to reviewer#1, we have explained how we would calculate the flux divergence directly from the airglow images. We would have to follow an individual wave to verify if it's visible in two layers simultaneously, then we would measure the MF of this wave in each layer, and finally subtract these values to have an estimation of the divergence for that specific wave. However, we have not done that in this paper.

Line 11 Mean MF, total MF and number of detected events

585.96/362 is not 0.88.

  - The reviewer is correct. We have updated the estimation to 1.62+-2.70 m^2/s^2.
  - We have realized that showing the total momentum flux of all waves detected brings more confusion (see reply to reviewer#1) and decided to remove that from the manuscript.

How is the mean estimated? Is the detected number 362 the number of independent wave events, or multi-counted number? The same comment to the lines 285-286.

- The waves are not necessarily independent, but it would be more likely that each detection corresponds to an independent wave detection.
- As we rely on a set of three images at the time from where we obtain two time-difference images, and finally the cross spectra from the 2DFFT of the time difference images. So, the time span of each set is about 30 min, and most of waves would have completely disappeared the imager FOV within that time span because the duration of a gravity wave is short based on our experience.

Lines 17-18

The lidar data in the upper stratosphere is not actually analyzed in the manuscript, but only qualitatively mentioned. This statement does not seem appropriate in the abstract.

- We have removed that.

The main body of the manuscript

Line 52 'modes'
Meaning not clear.

- We have reworded the sentence for clarity.

Line 58 'large amplitude filtered wind fluctuations' Meaning not clear.

- We have removed the word filtered to avoid confusion.

Line 84 'long period oscillations'
The wave structure is not very clear. Even one cycle is hard to distinguish, especially for the Nov. 06-07 case.

- The Nov 6-7 case is less pronounced, but can be seen in the zonal keogram around 1200 UTC . We have overlayed ellipses to make it easier for the reader to identify the airglow structures. It is clear that we have only considered these structures because they have also caused pronounced fluctuations on the wind fields and are associated with those large-scale waves, otherwise it would be hard to prove and explain that they would be gravity waves indeed.

Line 91 'time difference'
Is this done using pairs of the adjacent 10 min separated images? The detail should be written.

- We have put details of the image processing in the appendix, one for the auto-detection method, and other for the keogram analysis. We hope this makes this part clear for the reader.

Line 116 'smaller' > shorter

- We have rewritten the sentence.

Line 116 'simultaneously the back.....'
'with' after 'simultaneously'

- We have rewritten the sentence.

Line 118 'Fig. 1c'
Meant to be Fig. 1d?

- It should be meridional keogram in Fig. 1c. The figure 1d refers to the small-scale waves (lh<725 km).

Section 3
The definition of 'small' and 'large' should be described at the beginning of Section 3. Sub-section 3.2

- We have done that as asked. The small-scale events refer to waves with horizontal wavelength <725 km, while large-scale events are considered here as having horizontal wavelength >725 km. The 725 km range corresponds to the diagonal line across the field of view of an image mapped into a 512x512 km^2 grid. This way, a 725 km wave would still be fully seen within the image frame (on crest, one trough).

The meaning of 'fluctuation' at line 182 is not clear although it is inferred later at lines 190-191. It is confusing. The filter characteristics also should be written in the caption of Figure 6.

- We have removed the word 'fluctuation' for simplicity since the result of the weighted wind calculation can be seen in the figure. The details of how the wind fluctuations were obtained are also added to the caption of Fig. 6.

Lines 210, 211, 219, 220, 224, 234, 235 316, 317, 320 and 321
Why are the uncertainly of all these values '+-1'?

- The uncertainty corresponds to the smallest division in the keogram temporal axis.

Line 244 'amplitude'
Since the background wind is not thought to be a wave, rewording will be appropriate; something as magnitude.

- We agree with the reviewer and have changed that.

Line 245

Absorption occurs at a critical level, but reflection occurs at a turning level. Different wind structures are responsible, perhaps as you know.

- There is confusion in the literature. I think as critical level the altitude where the wave could be absorbed or reflected, as the word 'critical' suits both. If we would specify further, then we should use turning level to the altitude where the wave is reflected, and absorption level the altitude where the wave is absorbed. It is much clear and gives no room for confusion. We have removed "critical" and use only absorption or turning lever to be precise of the meaning we want to convey.

Lines 283-284 'toward the west of -0.36+-1.51 m2/s2' Very confusing description.

- We have detailed further the explanation.

Lines 286-288 The finding of a small number of waves carrying a large portion of MF is a good point. I suggest that the authors include discussion on GW intermittency and its importance in model atmosphere studies.

- We have added the discussion about wave intermittency.

Lines 289-294

This can largely affect the obtained results. Hopefully more discussion wanted. Isn't there any possibility that the layer thickness is related, or is it already taken into account in the analysis? It seems from Figure 4 that O2 layer is the thinnest.

- Wave detections in separate layers do not rely on the information about layer thickness or layer altitudes but only in the amplitude of the wave that must be large enough to produce a prominent peak in the cross spectrogram of amplitude. Thus, those features (layer thickness and altitude) hardly would influence the results. However, the fact that large amplitude waves are seeing in the O2 layer is surprising given the layer overlapping structures. This must be investigated separately. At this point we don't have a good explanation and providing one right now would be pure speculation. However, the O2 has the narrower estimated FWHM for the campaign, and that would allow shorter vertical scale waves to be seen in the O2 images, and consequently larger momentum flux waves would be measured there (see lines 311 -313).

Line 296

Yes, if the acceleration or deceleration occurs all along the same latitude circle, to my understanding.

- We could not fully understand the reviewer point of view here. We could provide a better answer if the reviewer is willing to elaborate further this comment.

Lines 339-340

I think this is a nice point. In the radar studies, a long-lasting topic has been which period range of GW is most responsible for MF deposition. Short period GWs were thought to be responsible before, but recent studies suggest that longer period waves are responsible. One example I know is Sato et al, 2017 (https://doi.org/10.1002/2016JD025834). There can be more. Including such preceding studies will be beneficial for even more fruitful discussion.

- We have added a discussion as suggested and also added the Sato et al. (2017) paper to the reference list.

Figure 2 '> 5 hours' should be '< 5 hours'?

- The reviewer is correct, although as explained before, there is not a hard cut off in the filtered periods given the way the fluctuations were calculated, that is, Wind fluctuations were obtained by first applying a 4-hours, 4-km temporal and vertical windows to get winds representing scales larger than these values. Then we subtract these estimates from the total wind field.

Figure 5

Are these dots independent wave events with each other?

- The dots are not necessarily independent wave events but are treated here as independent waves here. That does not affect the average momentum flux because, by clustering the wave events detections into independent wave events, we would have to calculate the mean momentum flux of each individual independent wave and then average the momentum flux of these independent waves in order to know the mean momentum flux during campaign or each night. We have indeed a clustering algorithm at does the job for us, but we decided not to do so in this manuscript.

- As we rely on a set of three images at the time from where we obtain two time-difference images, and finally the cross spectra from the 2DFFT of the time difference images. So, the time span of each set is about 30 min, and most of waves would have completely disappeared the imager FOV within that time span because the duration of a gravity wave is short based on our experience. This way, it would be more likely that each detection corresponds to an independent wave detection.

Figure 6

Meaning of 'fluctuation' should be described clearly. High pass filtered?

- As per request of the reviewer, we have added to the figure caption a short explanation of how the fluctuations have been obtained from the total wind field.

Figure 7

I am afraid that a spectral analysis after applying a filtering is not acceptable.

- We should not have referred to that as "filtering" because reader will think it as a digital filter operation. Here is how we did it: The total wind field was obtained by processing the raw meteor radar data using a 30-min, 1 km window. To calculate the wind fluctuations, the raw meteor radar data was processed using 4-hours, 4-km averaging windows. Then result was than subtracted from the total wind field resulting in the wind fluctuations associated with gravity waves. We have corrected this in the paper to make it clear for the reader what has been actually done to obtain the wind fluctuations.
- We believe the spectral analysis of the wind fluctuations is not faulty. We did not explain correctly how the wind fluctuations were calculated, but this issue is fixed now. Figure 7 shows indeed the relevant wave amplitudes during the campaign, even though we could not suppress completely the tidal modes. A significance threshold line (99% confidence) has been added to the plot in figure 7 to show the relevant wave amplitudes and periods.
- We have addressed the issue with the filtering of the horizontal wind for the wind fluctuations. The filtered wind is used to compare with the large-scale waves in the airglow keograms. For correcting the wave period Doppler Shift, we use the total wind at the moment of wave detection, not the filtered wind nor the fluctuations.

Figure 8

Image data and wind data should be treated in a similar manner; detrend, background removal or whatever.

- The images were detrended before spectral analysis, and also the keograms. The Wing fluctuations already have mean close to zero and no trend, as it is seen in figure 6b.

Figure 9

The way of 2D spectral analysis should be described in the manuscript.

- We Have added the 2D spectral analysis of keograms in the appendix, where we describe completely how the analysis is carried out. we have also added another appendix session to explain further how the auto detection method works. We hope that this will make the paper more self-explanatory, avoiding to relying on separated publications.

Figure 10

If all the figures are processed with the high pass filter with the cutoff of 5 hr, reprocessing is suggested, at least, for the November 6-7 case.

- That is not really a digital filtering operation. We have included the following in the text to make clear how we carried out the wind processing: "To obtain the wave fluctuations (Fig2b), we first use 4-hours, 4-km temporal and vertical windows to get winds representing scales larger than these values. Then we subtract these estimates from the total wind field. The total wind field was calculated using smaller temporal and vertical windows, that is, 30 min and 1 km, respectively. By doing that we reduce the contributions of large-scale winds, nonetheless the resulting fluctuations still keep some of the energy of larger periods waves as can be seen in the spectrum."
- As we have explained before, the Nov 6-7 case is less pronounced, but can be seen in the zonal keogram around 1200 UTC. It is clear that we have only considered these structures because they have also caused

pronounced fluctuations on the wind fields which are associated with those large-scale waves, otherwise it would be hard to prove and explain that they would be indeed gravity waves

Interactive comment on "Mesospheric gravity wave activity estimated via airglow imagery, multistatic meteor radar, and SABER data taken during the SIMONe–2018 campaign" by Fabio Vargas et al.
Anonymous Referee #3
Received and published: 23 October 2020
The comment was uploaded in the form of a supplement: https://acp.copernicus.org/preprints/acp-2020-896/acp-2020-896-RC3- supplement.pdf

General comment:
The authors describe different measurements they carried out during the SIMONe-campaign in November 2018 at or around Kühlungsborn, Germany. Supplementing satellite-based data are used. They combine the measurements in order to fully characterize gravity waves and discriminate between large and small-scale waves. However, they do not explain what they understand under small and large scale.
From my point of view, there are two main results. The authors found out that approximately 11% or all detected waves carry ca. 50% of the total momentum flux and they had a specific look on two large wave events. They motivate that these structures might be due to secondary gravity waves. Nevertheless, this remains speculative.
The manuscript is well-structured and sections 1 to 4 are easy to read in the first approach. However, on closer inspection important information is missing. In section 5, the formulas disturbed my flow of reading. Following the classical approach, they should appear earlier in the manuscript which would help here. The data and the methods used to measure and identify the gravity are appropriate, however especially the data section could have some more details. My main point concerning the section results refers to error bars and/or significance levels: I didn't find a single one.
I propose to accept the manuscript after some major revision.

- We thank the reviewer for raising important comments about our paper and for taking the time to do so. We appreciate your help very much.

Major points
The manuscript is written in a rather abbreviated style.
The most important point in this context is that the manuscript suffers from a lack of information about the quality of data and analyses.

- We understand the reviewer's concern about having written the manuscript in an abbreviate style. Maybe because we wanted to make it concise, we have failed while describing important parts of the analysis and processing, which must be done precisely to permit the reproduction of the results.

I found neither a single error bar nor a significance test in the section results (in the discussion part there are very few error bars). For clarity issues, it is probably not helpful to provide this information directly in all figures (for example I have no idea how to incorporate error bars in keograms), but it can be done in some cases (FFT) and in the others the information can be given in the text. Parts of the main results depend on statistical analyses.

- The incorporation of error bars in the spectral analysis could be found from our simulations of the error propagation into gravity wave parameters in our recent paper (Uncertainties in gravity wave parameters, momentum fluxes, and flux divergences estimated from multi-layer measurements of mesospheric nightglow layers, https://doi.org/10.1016/j.asr.2018.09.039.)

A second point in the context here is that the authors do not explain how they define wave event and which consequences this definition has on their results. If I operate an imaging system which takes a picture every ten minutes, is each result of the spectral analysis of each image defined as a wave event or is a wave event an oscillation in space which shows nearly the same horizontal wavelengths over some time (so in some images). Fast waves would be underrepresented in the first case. Does this have any influence on the results?

- For the small-scale analysis using the autodetection method, we have defined as a gravity wave event the output of the cross-spectrum of two time-difference images when the special peak is larger than 10% of the total energy of the spectrum. Two time-difference images are generated from three light frames of the airglow (please take a look at fig 01 for Vargas et al 2009 (https://angeo.copernicus.org/articles/27/2361/2009/) showed here below:

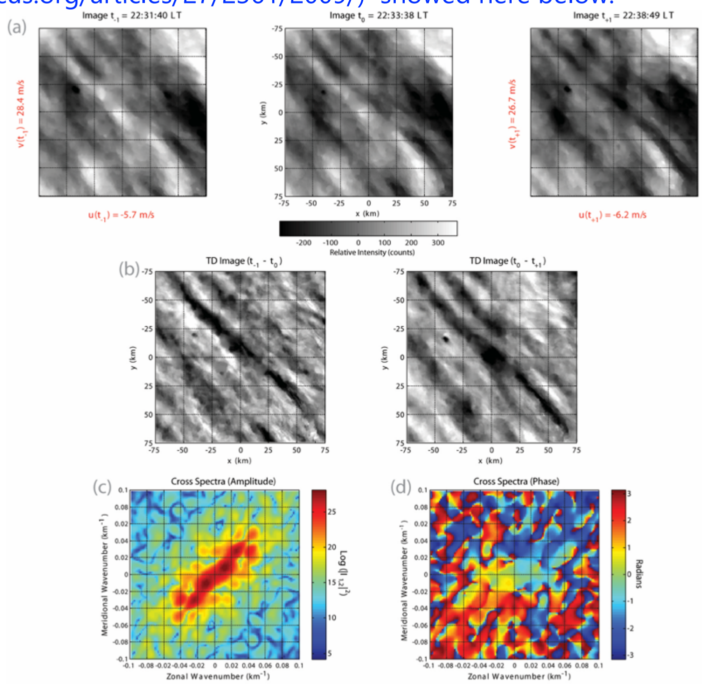

Figure 1 Processing of a set of three airglow images in order to obtain the cross spectra. In (a) it is showed a set of sequential OH images presenting GW structures. (b) Time difference images obtained from the set of images. (c) Amplitude cross-spectra of the TD images, from where we estimate the wave amplitude, propagation direction and horizontal wavelength. (d) Phase cross-spectra of the TD images showed in (a).

- Thus, if a wave is detected in a given set, it is considered an independent wave detection. Now, if in the next set another wave detection is made, the only way to tell the two events to correspond to the same gravity wave is by comparing their wave parameters. Now, the momentum flux of a wave varies as it goes through the field of view. thus, considering the momentum flux average of all the waves detected during the campaign would be the same as clustering the corresponding wave events into a distinct wave, and then averaging the momentum flux for that specific one for the duration of the event over the airglow images where it shows up, and then averaging over all the distinct wave events, just would be more laborious. We have a clustering algorithm that does work for us, but still, we choose not to do it here.
- Again, we rely on a set of three images at the time from where we obtain two time-difference images, and finally the cross spectra from the 2DFFT of the time difference images. So, the time span of each set is about 30 min, and most of waves would have completely disappeared the imager FOV within that time span because the duration of a gravity wave is short based on our experience. This way, it would be more likely that each detection corresponds to an independent wave detection.

Another point is: It is really strange to see a paper where TIMED-SABER data are used and Martin Mlynczack and James Russell (or at least the SABER team in general) are neither co-author nor mentioned in the acknowledgements. There isn't even a single citation of them (e.g. Russell et al., 1999, https://doi.org/10.1117/12.366382 or Mlynczak, 1997, https://doi.org/10.1016/S0273- 1177(97)00769-2). On the other hand, there exist co-authors here who also "only" delivered data. This is not consistent. Maybe the authors offered co-authorship to the SABER people and they declined, I don't know that, but is there really nothing to mention in the literature list or in the acknowledgements?

- Regarding the SABER data, we did not acknowledge the SABER team in the proper section, but we should have. We clearly thank the SABER team now in the acknowledgements statement. We have not offered coauthorship to the SABER team indeed and are not aware coauthorship is required to use SABER data. We think an acknowledgment note will suffice. We have also included the suggested references to the list and made citations at proper locations.

Minor points

Section 1

General comment: The introduction is quite general. In my opinion, the technical focus of this manuscript is on the combination of different measurements to describe gravity waves as comprehensively as possible. Airglow imagers are used in order to derive horizontal wavelengths and periods. Wind information come from radar data. Temperature information are based on SABER data. Other groups have already done such studies or similar ones - just enter 'airglow radar SABER gravity waves' in google scholar. However, there is no reference in your manuscript. One of the main topics of the manuscript is the derivation of the momentum flux. There are already other publications on this topic which are not mentioned here or in the discussion (e.g., Ern et al., 2011, https://doi.org/10.1029/2011JD015821 derived the momentum flux globally based on satellite data). Please include some citations and put your work into the context.

- We have included citation of other references including momentum flux derivation in the introduction section, including that on of Ern et al, 2011 and others we could find.

p. 2 l. 48 Can you please provide the exact campaigns period?

- We have done so.

p.3 l. 55 & 57 What is small and large scale for you? This comments also refers to the headings of section 3.1 and 3.2.

- The small-scale events refer to waves with horizontal wavelength <725 km, while large-scale events are considered here as having horizontal wavelength >725 km. The 725 km range corresponds to the diagonal across the field of view of an image mapped into a 512x512 km^2 geographical grid. This way, a 725 km wave would still be fully seen within the image frame (on crest, one trough). We have also included these specifications in the text.

Section 2

From my point of view, the level of detail of the different subsection varies (2.2 has more details than the two other subsections). Additionally, I do not get all "classical" information for all instruments such as spatial and temporal resolution or some information about the data quality (not necessarily bias and precision but for example comparisons with other instruments, for SABER such studies are available).
I also miss further literature for ASI and SABER where the reader can look up (technical and data processing) details about the instruments (e.g. concerning ASI the detector size etc., concerning SABER the retrieval etc.).
For SABER, different data versions exist. I conclude from the legend of figure 4 that you use the newest one (2.07) but not every reader might be familiar with the "SABER notation", so please provide this information also in section 2.3.

- We have done our best to attend your request.

p. 4 l. 87 In the text you use UTC, in figure 1 you use p.m. If it was consistent it would be easier to read.

- We understand your concern, but, respectfully, we have decided to keep it as is because this minor issue will not affect the interpretation of the plot and the results of the paper.

p. 4 l. 94 You write that the result of a time-difference operation is an image where the contrast of small-period, small-scale oscillations is enhanced. I think with small-scale you mean the spatial dimension. In this case, I do not fully agree with you. Whether you enhance a signature or not should depends on the speed of the signature: if it is near zero you won't see it in your time-difference image because you just subtract it. The phase speed is directly proportional the wavelength (in this case the horizontal one) and indirectly proportional to the wave period. The phase speed significantly differs from zero, the larger the wavelength or / and the smaller the period is. So, you enhance small period but large-scale oscillations.

- The reviewer has presented a good point. Our definition of small horizontal wavelength (lh) wave considers lh<725 km. Once the detections correspond to waves of small periods (<60 min) and lh<150 km, our statement of small period small horizontal scale waves is consistent. The plot below (figure 2) shows a calculation of how the TD operation would affect the wave amplitude as the wave period vary. It shows the ratio between the actual wave amplitude (A) in the original image to that on the TD image (A_T). We considered the sampling period of 2 minutes. In the plot, we see the wave amplitude decays to < ½ of that the original wave amplitude for periods larger than ~25 minutes. So, the larger periods waves must present strong amplitudes to be detected by the time-difference method.

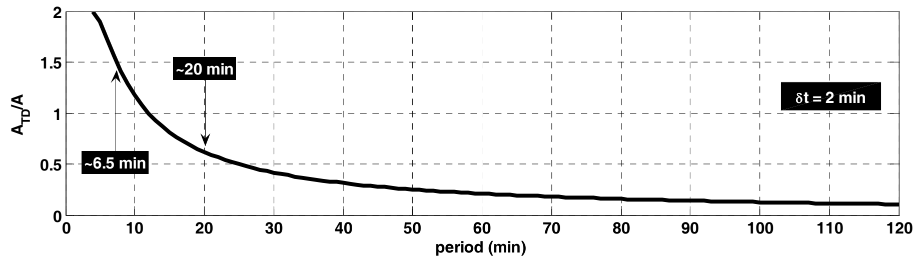

Figure 2 Ratio between wave amplitudes observed in a TD image and in an original image as a function of the intrinsic period of the wave. The sampling period used to compose this graph was 2 minutes.

p. 4 l. 115 Which high-pass filter exactly? If you say you use a five-hour high pass filter, it means for my that all periods longer than five hours can pass. Later in the document, it becomes clear that the opposite is true and you probably referred with the term "high-pass" to the frequency domain. Can you please clarify here which periods are still present in the filtered data. Additionally, in the spectra in figure 7 you still see a rather dominant p. 4 l. 118 Are you sure that you really see exactly this oscillation?

- We should not have referred to that operation as filtering because reader will think as a digital filter operation. Here is how we did it: The total wind field was obtained by processing the raw meteor radar data using a 30-min, 1 km window. To calculate the wind fluctuations, the raw meteor radar data was processed using 4-hours, 4-km averaging windows. Then result was than subtracted from the total wind field resulting in the wind fluctuations associated with gravity waves. We have corrected this in the paper to make it clear for the reader what has been actually done to obtain the wind fluctuations.
- From this, it is clear that oscillations of periods longer than 4 hours will be suppressed, but not completely eliminated. Also, waves having vertical scales <4 km will be suppressed, but not completely eliminated in the resulting wind fluctuations. The spectra in figure 7 reflects the fact that not all longer period oscillations were eliminated, but it doesn't mean the spectra is incorrect. We also can tell what peaks are associated with gravity waves once waves of similar periods are also seen in the keograms.

p. 5 l. 120 The abbreviation SABER is not explained in the manuscript.

- We have explained the abbreviation earlier in the manuscript when we first mention the acronym SABER in line 59-60.

p.5 l. 127 Please concretize the lapse rate you mean.

- The reviewer has asked to explicitly give the value of the lapse rate, is that correct? See lines (131-133.

p. 5 l. 127 Please be a little bit more precise here. It is not important that the orbit of TIMED is exactly over the observatory, the field of view of the instrument has to measure over or near the observatory.

- We have elaborated more. The specific fragment now reads "Even though the satellite orbits registered during SIMONe-2018 were not exactly over the observatory, the instrument measurements are performed in limb vertical plan that is near or within the field of view of the imager (Fig. \ref{fig03}), where the colored dots indicate where the measurements are being made, not the satellite position"

p. 5 l. 128 From figure 3 it looks like you use also profiles which were not within the field of view of the imager.

- The reviewer is correct. We have used all the measurements we could find to diagnose the background atmosphere stat in the nighttime period during the campaign.

p. 5 l. 133 It is great that you are able to calculate the VER profiles for the different species but why don't you use the ones provided by SABER?

- The reviewer is correct. That is because we did not want to mix in the analysis the use of measured profiles with the calculated profiles. It would not cause a big change in the results; thus, we carried out the analysis using only the calculated profiles.

p.5 l 137 Please correct the letter shift (FWMH→FWHM) and explain the abbreviation.

- We have done so.

Section 3.1

The way to present such campaign results is always a tightrope walk. If the reader is flooded with details, he loses the overview, if it is too short, questions remain open. For me questions remain open.

I miss two formulas (dispersion relation for high-frequency waves and vertical flux of horizontal momentum, or at least citations of literature where the reader can look them up) and in the case of the dispersion relation I would like to read some information about the Brunt-Väsälä frequency (probably calculated based on SABER, VER weighted?).

- We have addressed the lack of explanation by providing two appendix sections where we detail the auto-detection method and the keogram spectral analysis for the readers.

Please also provide the information that the cross-spectrum is the Fourier transform of the cross- covariance function, since you treat pictures you probably use the 2D version. Another useful information would be the sensitivity of the analysis. You calculate the cross-covariance of two TD images. The calculation of TD images already means filtering the data for fast waves. The calculation of the cross-covariance provides you information about the waves which change from one TD image to the other. So, there are two stages of filtering and it would be interesting to provide information which waves pass this filter, and which don't.

- The reviewer is correct, we have indeed used do 2D Fourier transform in each time difference image and then combine the spectrum of these two obtaining the cross spectrum the figure 1 above shows the process clearly.
- One thing that is not clear in the figure is that we have correct the images (shifting pixels) to account for the wind velocity across the field of view, that is, we have performed the Doppler shift correction in the wave period already. This process is depicted in the figure 3 bellow. Notice the red arrows indicating the shift in a bright spot of the image.

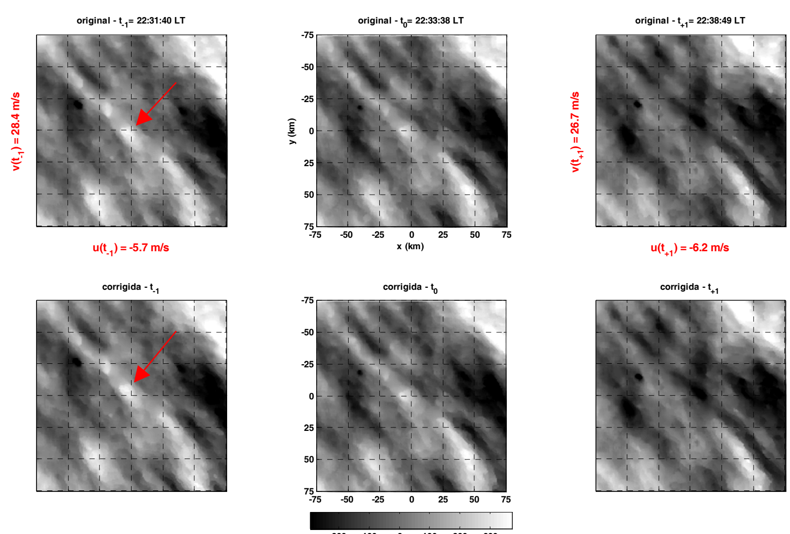

Figure 3 Doppler shift correction by moving pixels in the processed image set

p. 6 l. 165: I think you mean 5j instead of 5e and the wavelengths range between 10 km and 40 km.

- The reviewer is correct. We have changed that accordingly.

p. 6 l. 169: I see 100 m/s instead of 80 m/s.

- We have changed that accordingly.

p. 6 l. 176: "larger momentum waves on Nov. 2-3 and Nov. 3-4." Ok, it's a log plot but the maxima of these two nights are not so much higher than the maximum of Nov. 1-2, for example, which brings me to the question of error bars. If you plot them, figure 5l might become a little bit busy, so this might not be the optimal solution, but in any case you should give information about the error bars somewhere (also concerning the other parameters shown in figure 5) and state whether the sentence about the date of appearance of the larger momentum waves is still valid in this case.

- We have calculated the error bars of each parameter of each wave event measured. These errors are calculated using the methodology developed in Vargas 2019 (https://doi.org/10.1016/j.asr.2018.09.039). We will provide the average error of these parameter in each plot for completeness. As the reviewer says, the plots will become busy if we insert error bars in each data point.

Section 3.2

p. 7 l. 184 "once the layer peaks within +/-2 km from each other"? The wind fluctuations weighted with the VER of O(1S) and OH(8-3), so figure 6 d and f, look really similar, even though the respective peak heights are more than 4 km away from each other.

- WE have doubled check our calculations and verify they are correct. The weighted wind fluctuations are similar indeed, but not identical. The similarity is related with the long vertical wavelength fluctuations that can be seen in Figure 2c and Figure 2d. we have added more explanation to the text (line 191).

p. 7 l. 185 The citation you provide refer to the equatorial region, you should mention at least one citation referring to mid latitudes (e.g., Wüst et al., 2017, https://doi.org/10.5194/amt-10-4895-2017).

- We have inserted the suggested citation.

In any case, 15 km is indeed large. When I look at figure 4 c (VER measured by SABER), I find values of 9 km to 11 km which is much more in the range of other authors. Your simulated profiles in figure 4d (thick lines) show higher values but none of them reaches 15 km. So, first I wonder where the 15 km FWHM comes from and then I would be interested in why is there a difference between simulated and measured values? Which one can I believe or are both ok within certain limitations? And now we are again in the range of error bars, quality of the data etc.

- We have explained in the text that the FWHM was calculated from a gaussian fit of each VER. The layer thickness is in a table 2 for all the simulated and observed VER. It is clear that we if we proceed in the same way as the reviewer, by measuring the FWHM directly from the graphs, we will have much shorter or narrower FWHM. We wanted to be consistent while composing Table 2 by using the FWHM from the gaussian fit of the VER curves.
- Also, the measured profiles could be affected by long period waves which would push the layer up and down and also boot cause it to be narrower or thicker depending on the phase of the perturbation affecting the layer. See figure 4 below of our simulation of how a wave causes the depicted effects in the redline layer from Vargas 2019 (https://doi.org/10.1029/2019JA027356):

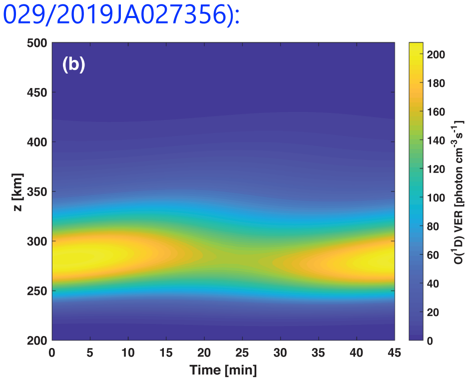

Figure 4 Time versus altitude cross section of the (b) perturbed O(1D) volume emission rate,

p. 7 l. 187 The values after the +/- are what?

- The value refers to the spread in the rms value of the wind.

p. 7 l. 189 I miss a significance level in figure 7.

- The significance level has been added and the text has been modified accordingly.

p. 7 l. 193 Please omit "salient" – this peak is as salient as the 12 h peak for example, which is only due to leakage as the authors say. By the way, I find it strange that peaks which are due to leakage are as prominent as others. Here, a significance level and more information about the filter as already mentioned before would help.

- We have removed the word salient and have added further details of how the fluctuations are obtained (line 196).

p. 7 l. 211 I find it difficult to see a period of 8 h±1 h.

- Evidently the wave is propagating zonally eastwards. The tilt in the brightness patch indicates how fast the wave is traveling in that direction, and because the tilt is small, we can only see that it is a small speed wave. To obtain the wave periodicity we had to rely on the keogram spectral analysis, but the keogram helps to verify the brightness patch is due to an 8-hours large-scale gravity wave, not an 8-hour tidal structure.

p.7 l. 215 Which spectral analysis? Please concretize.

- We have added more explanation in the appendix section to show how the spectral analysis of keograms was carried out. We also have put that on the text.

p. 7 l 217 The keogram analysis does not only provide horizontal wave numbers, you also mention the wave frequency in figure 9. Can you please concretize this in the text? Furthermore, you mention the observed frequency $\hat{\omega}$ in the text but the frequency ω in figure 9. You probably mean the observed frequency in figure 9, don't you?

- We have done as asked. Yes, figure 9 refers to the observed frequency. We have corrected the symbol in the figure and in the figure caption. We perform doppler correction in the wave period later on using the background wind in order to estimate the large-scale waves momentum flux.

p. 8 l. 118 &v226: Is there a difference between ~0 and 0.0×10-3 within the unknown accuracy of your analysis and the unmentioned significance levels?

- Based on our auto-detection method, the significance level for a spectral peak to be considered as a wave event is that the sum of the spectral energy around the spectral peak is larger than the total energy of the spectrum. Fig 9b and 9c show that for different waves, the spread of energy around the peak is different, so the uncertainty of each one depends on the spread, where the threshold wavenumber is at where the energy sum around the peak is <10%. For more information, please refer to Vargas 2019 (Advances in Space Research 63 (2019) 967–985)

p. 8 l.228 & 230: You mention that the phase is propagating downward but the wave is propagating upward? Don't you mean the energy is propagating upward?

- We know that gravity waves are dispersive type of waves, and because that, if the wave packet is propagating upwards, that is also the direction of energy propagation. In our view, we could use one way or another interchangeably.

Section 4

p. 8 first paragraph: you argue that the atmosphere is convectively stable using the mean temperature profiles over some days. When discussing dynamic instability, you look at individual measurements and argue that they can reach 50 m/s and more. This is not consistent having the mean on one side and the individual profiles on the other. Please go a little more into detail here. Furthermore, you write that since the wind field is rather strong it could cause critical levels – wind fields can always cause critical levels. It just depends on the phase velocity of the wave. You probably mean that large wind speeds are more likely to cause critical levels.

- The reviewer is completely right regarding the discussion about the wind velocity. Actually, the wind shear above 40 meters per second per kilometer would be the cause of dynamic instabilities. We have rephrased the sentence to read "Thus, gravity wave dissipation due to convective instabilities would not affect the vertical evolution of the gravity wave field during the campaign. We have also verified that dynamic instabilities did not occur because the wind shear was <30 m/s/km most of the time during the campaign. On the other hand, because the horizontal winds occasionally achieved relatively large magnitudes >50 m/s (Fig.02a and Fig.02b), the wind field could have caused absorption of waves having phase speed <50 m/s traveling to the same direction of the wind vector."

- We have removed "critical" and use only absorption or turning level to be precise of the meaning we want to convey, once we believe "critical" causes confusion for readers not aware of the details of gravity wave propagation in vertically structured atmosphere.

p. 8 second paragraph: You write that the wind is controlling the propagation of southeastward waves via dynamical filtering and draw this conclusion from the comparison of two figures, one addressing the momentum flux direction (figure 5a) and the other showing the wind direction (figure 5k). Why don't you conclude this from the comparison of figure 5f and k? Figure 5a tells you only that there is not much momentum transported in southeastward direction, but this can be due to too "weak" waves or too few waves or a mixture of both.

- WE could have done so from figure 5f and k, but we wanted to show that looking at the momentum flux azimuth chart is not enough to tell that the wind is controlling the horizontal propagation direction, once the wave propagation direction azimuthal histogram still shows waves moving into the wind.

p.9. l. 253 You mention a wind speed of ca. 39.3 m/s. Is this the mean over the background wind or over the total wind (including the gravity wave signatures)?

- 39.3 ±18.9 m/s m/s refers to the wind speed mean and standard deviation in the southeast quadrant sector (270 to 360) in Fig. 5 k. (we have now stated that in the text in lines 264-265).
- The mean wind speed on the 270-360 degrees quadrant corresponds to the background wind.

p. 9 l. 253 & 254: the number behind the plus-minus sign is the standard deviation?

- It is the standard deviation of the sample.

p.9. l. 255-281: you compare your results to two other publications, one of them is a PhD thesis and not peer reviewed I assume. It is not clear to me why only these two publications are suitable for comparison. There exists a number of other studies since 2011 just type 'airglow gravity waves horizontal wavelength' in google scholar, even if you restrict your search to 2016 to 2020, you still get many results - not all of them might deliver all wave parameters you derived but even in this case there exist some. So, could you please extend your comparison here accordingly?

- We have done so as per your suggestion and the other reviewers as well.

p.9. l. 256: You write that your results are directly comparable to Li et al. (2011) since they used a similar auto-detection method. However, you say nothing about the sensitivity of the instruments, which is used by those authors, to the different horizontal wavelengths. The sensitivity of an airglow imager should be determined by the field of view and the number of pixels your imager has, for example. As you mention in line 265 also other parameters such as filter wheel cycles or integration time determine the sensitivity. Can you please adapt the formulation in the manuscript accordingly?

- As far as we know, the Li imaging system was not calibrated for sensitivity, Notice the Li system is the same used in ALO, Chile, since 2009, and we have total understanding of the system details. The IAP imager system is also not calibrate for sensitivity.

p.9 l. 267: Please replace min by minutes

- We have replaced "min" to "minutes" in the whole manuscript.

p.9. l. 269: You write that the filter wheel cycle which is used does not only influence the derived periods, it seems to influence also intrinsic phase speeds. It should! Phase speed is related to the ratio of wavelength and period. The filter wheel cycle influences the sensitivity of your measurement system in the temporal domain, it does not affect the spatial domain. If you can detect waves which are characterized by smaller periods but by horizontal wavelengths in the same range than before, you will automatically see faster waves.

- We have included that in the text to make the readers aware of that as well in lines 284-286.

p. 9 l. 275-277 Can you please provide citations here or is this information taken out of Li (2011)?

- The statement is based on our personal experience observing gravity waves with ALO airglow imager at ALO, Chile, over 10 years, although Li (2011) provides the only study to date discussing the small-scale waves. Another study from our collaboration with a Chilean university has been submitted but is still under review, and maybe can be include in the citation list if gets published sooner.

p.9. l. 280 Convective sources during winter? Ok, we could think about strong low-pressure system but since you do not bring further arguments here, can you please mark this sentence as speculation?

- We have in fact found satellite images for some of the days during the campaign presenting large convective structures to the north (over Oslo) and west (over Netherlands) of the observatory. We did not used those figures in this paper because we want to write another paper that questions the origin of the observed waves, including the possibility of secondary wave mechanism (based in lidar measurements) generating the observed large-scale ones.

p.10 l. 293 & 294 Your vertical wavelength is in the range of the FWHM. According to table 2, the O2 layer is characterized by the smallest FWHM compared to the other layers you observed. So, I would assume the strongest signal in this layer.

- We have added the following to that sentence: "It is not clear why the enhanced waves are seen most in the O2 emission once the layer's peaks nearly overlap, but this could be related to the fact that the O2 VER has the smallest FWHM (see Table 2). These shorter λz waves would be seen in images of the O2 emission primarily, and their momentum flux would be larger for it increases as λz decreases (see Fig. 5i)".

p. 10 l. 208 You left out 1/4H2 where H is the scale height. Please mention this. Did this omitted factor contribute to the error bar (given in l. 316) or is it not necessary?

- Using the full dispersion relation, the error in the vertical wavelength (lz) has been estimated in our work Vargas et al. 2019 (Advances in Space Research 63 (2019) 967–985). We have found there that the error in lz can is large because it depends on other variables that are also estimated and have errors. For instance, for a 10 % error in the horizontal wavelength and 10% error in period, the error in lz would be about ~20%. Also, we don't know exactly where the airglow layers peak, and the altitude of the layer also impacts on the lz estimation and in the lz error. We have omitted the term 1/4h2 because it causes only ~5% difference compared to the reported value, although we have revised the error to be 20% at this time.

p. 10 l. 316 I wonder where the error bar comes from since you didn't provide any error bars in your analysis. Please comment.

- WE did a visual calculation of the vertical wavelength and have assigned an error of 1 km to that measurement that is ~2x the size of the vertical resolution (0.5 km) in Fig.10.

p. 11 l. 328 Please substitute m/s by m/s2 when writing about g.

- We have corrected that.

Section 5

p. 12 l. 362 Where do these numbers come from? I find 22-41 m/s/day in the manuscript and this is for the assumption that the wave breaking continues for 24.

- The numbers come from Figure 9e of Vargas et al. (2007) for waves having lz = 20-25 km and lh ~ 100 km that are the 11% of the observed small-scale waves carrying more than 50% of the total observed flux in our study. We have explicitly state that in the paper now.
- Yes, that is in the case the wave breaks for 24 hours, which is an estimation. But it is likely the waves will die out earlier, so the impact of a specific wave does not last longer.

Section Acknowledgements

p.12 l. 378 Which ftp?

- We have included the link for downloading the data.

Figures

Figure 2

It would be nice to provide the hint that the y-axis of a and b are different to the ones of c and d. Non- radar people might further appreciate a note explaining why there is a daily cycle in the length of the vertical profiles.

- The daily cycle is associated to the number of meteors been measured at time throughout the day. The meteor density is larger at earlier morning ours and smaller at afternoon hours. Because the wind calculation relies on the number of meteors to obtain a quality wind data, when there are not enough meteors the wind cannot be calculated. This is reflected in the plot as the given daily cycle at certain altitudes (z<80 km and >100 km). We have added explanation of that in the paper.

Figure 3

This figure is a challenge. I hope I can explain my confusion and I think you can solve most of it by just showing the respective fields of view and not the values measured within the fields of view. First of all: what do the colours in the rectangle and in the ellipse mean, you do not have a colour bar or maybe two?

- The colors in the rectangle is the pixel intensity of the airglow image (we can provide a color bar for this one). The ellipse shows the radar FOV and its colors reflects the meteor density (maybe not a good idea to show the color bar for this one, which would make the plot a little busy. We have removed the MR colors to avoid confusion.

The measurements shown are taken at which day?

- The measurement corresponds to different SABER orbits during the week of the campaign, specifically, DoY 307, 308, and 312.

I think the rectangle shows the imager but isn't the field of view of an all-sky imager a circle or a kind of ellipse when projecting it on a map with an equidistant lat-lon grid? You probably have just cut the area.

- The FOV of raw airglow images are indeed like a circle. During pre-process, the image is mapped into a 512x512 km^2, rectangular grid of pixels with resolution of 1 km/pixel. The lat-lon grid in the figure was then scaled to match the mapped airglow image as 1 degree in latitude and 1 degree in longitude do not correspond to the same distance.

Then: on the right hand-side of the plot where only the ellipse covers an area (not the rectangle), there is a kind of border. This effect also appears the bottom of the plot. It does not appear where the ellipse ends and only the rectangle covers an area. Why? Maybe you plotted the rectangle over the ellipse.

- We want to preserve the shape of the rectangle to show that the imager FOV. The ellipse is the MR FOV and the center is not the same of that the imager once the MR system operates at other location away from the imager site. We again scaled the MR FOV onto the image rectangle.

Last: Please insert a y-axis labelling. Puh!

- We have done that.

Figure 4

a) Can you please provide the different SABER profiles in different colors or line styles or ...? I wanted to find out more about the static stability at individual days, but this is not possible if all profiles have the same color and line style.

- We have added colors and line styles to help telling apart the different profiles.

Please provide explicitly day of the year and UTC. I can extract it from the legend, but this might not be clear for everybody.

- We have done that.

c) Can you please scale the x-axis in a way that all profiles also the individual ones are completely within the plot?

- We have done that as well.

Figure 5

a) What do you mean with momentum flux versus propagation direction? If I plot y versus x, I have two axis. You also have two "axis" (one is the radius and one the direction) but the radius seems to show the number of waves or wave events.

- The radial coordinate shows the magnitude of the momentum flux in Fig. 5a. The momentum flux scale is written between 60 and 90 degrees. Notice the larger momentum flux events are moving towards 120 degrees, having magnitudes of ~25 m2/s2.

c) The value after the +/- is the standard deviation? About how many waves do we talk?

- The reviewer is correct. We have measured 362 events during the campaign, although some wave events are not necessarily independent. Some events could have been clustered was a single, individual event since the same wave could be seen in multiple image sets (1 image set = 3 sequential images). We have not clustered the events for this study.

d) j) and m) What is a wave event, so is it the result of one FFT or do you group the results of your FFT, e.g. if a wave is found in one FFT and a wave with rather similar parameters is found in the next FFT, is it the same wave or do you count it twice? Would it make sense to count it twice or would you include a bias in your statistics when counting it twice since fast waves will be counted less often than slow waves?

- Again, some wave events are not necessarely independent. As the reviewer notice, a bias could have happened if we were to analyze and FFT single images at the time. However, we rely on a set of three images at the time from where we obtain two time-difference images, and finally the cross spectra from the 2DFFT of the time difference images. So, the time span of each set is about 30 min, and most of waves would have completely disappeared the imager FOV within that time span, meaning that the same wave would likely not be detected in the next set of three images. This way, it would be more likely that each detection corresponds to a different, independent wave detection (line 315-320).

m) There is a strange white triangle in the lower right corner.

- It must have been a glitch of the software while coloring the bar of the histogram.

Figure 6

It would be better to extend the y-axis range especially in part (d) to (f) since especially at Nov. 7th the values are not shown in the plot anymore.

- WE have fixed that.

Tables

Table 2

The FWHM I read from figure 4c is roughly 9 km and 11 km for SABER mean VER profiles (thick green and thick black line) – why is there a difference to the values given here?

Here, I come back to one of my earlier comments. You simulate the layer but you also show values measured by SABER. How do I have to judge the differences? For example, you simulate another OH transition than you measure. The different OH transition dominate at slightly different heights (see e.g. von Savigny et al., 2012, https://doi.org/10.5194/acp-12-8813-2012).

- We have simulate the VER profile for the OH(8,3) using the SABER mean temperature and atomic oxygen for the campaign. I believe the difference between the simulated and measured lies on the average we have used in the simulation. I mean, to calculate the OH(8,3) VER, we rely on the mean temperature and atomic oxygen profiles. I believe the SABER OH and simulated OH VER would be much closer in structure if we have used single T and O profiles for the simulation, although we have not checked that here. We should include this explanation in the paper as well.

Compare Results

Old File:		New File:
airglowPaperIAP.pdf	versus	**revised_airglowPaperIAP.pdf**
27 pages (12.84 MB)		**35 pages (9.43 MB)**
8/26/20, 10:30:47 PM		12/12/20, 12:28:03 AM

Total Changes

538

Text only comparison

Content

262 Replacements

146 Insertions

130 Deletions

Styling and Annotations

0 Styling

0 Annotations

Go to First Change (page 1)

Mesospheric gravity wave activity estimated via airglow imagery, multistatic meteor radar, and SABER data taken during the SIMONe–2018 campaign

Fabio Vargas[1], Jorge L. Chau[2], Harikrishnan Charuvil Asokan[2,3], and Michael Gerding[2]

[1]Department of Electrical and Computer Engineering, University of Illinois at Urbana-Champaign, Urbana, IL, USA, 61801
[2]Leibniz Institute of Atmospheric Physics and the University of Rostock, Kühlungsborn, Germany, 18225
[3]Laboratoire de Mécanique des Fluides et d'Acoustique, CNRS, École Centrale de Lyon, Université Claude Bernard Lyon 1, INSA de Lyon, Écully, France

Correspondence: Fabio Vargas (fvargas@illinois.edu)

Abstract. We describe in this study the analysis of small and large horizontal scale gravity waves from datasets composed of images from multiple mesospheric airglow emissions as well as multistatic specular meteor radar (MSMR) winds collected in early November 2018, during the SIMONe–2018 campaign. These ground-based measurements are supported by temperature and neutral density profiles from TIMED/SABER satellite in orbits near Kühlungsborn, northern Germany (54.1°N, 11.8°E). The scientific goals here include the characterization of gravity waves and their interaction with the mean flow in the mesosphere and lower thermosphere and their relationship to dynamical conditions in the lower and upper atmosphere. We have obtained intrinsic parameters of small and large-scale gravity waves and characterize their impact in the mesosphere via momentum flux (F_M) and momentum flux divergence (F_D) estimations. We have verified that a small percent of the detected wave events are responsible for most of F_M measured during the campaign from oscillations seen in the airglow brightness and MSMR winds taken over 45 hours during four nights of clear skies observations. From the analysis of small-scale gravity waves (λ_h <725 km) seen in airglow images, we have found F_M ranging from 0.04–24.74 m^{2}s^{-2} (1.62±2.70 m^{2}s^{-2} on average). However, small-scale waves with F_M >3 m^{2}s^{-2} (11% of the events) transport 50% of the total measured F_M. Likewise, wave events of F_M >10 m^{2}s^{-2} (2% of the events) transport 20% of the total. The examination of large-scale waves (λ_h >725 km) seen simultaneously in airglow keograms and MSMR winds revealed relative amplitudes >35%, which translates into F_M =21.2–29.6 m^{2}s^{-2}. In terms of gravity wave–mean flow interactions, these large F_M waves could cause decelerations of F_D =22–41 ms^{-1}/day (small-scale waves) and F_D =38–43 ms^{-1}/day (large-scale waves) if breaking or dissipating within short distances in the mesosphere and lower thermosphere region.

1 Introduction

Atmospheric gravity waves represent a class of atmosphere oscillations where buoyancy is the restoring force. This class of waves transport momentum and energy over large distances within the atmosphere and have as primary sources troposphere disturbances like flow over topography, convective systems, or jets (e.g., Vincent and Alexander, 2020). To preserve kinetic energy, the amplitudes of the gravity waves grow nearly exponentially as they propagate upward into less dense air at higher altitudes. Because these waves break and dissipate, they deposit their momentum and energy into the background atmosphere. This affects the atmosphere over a broad range of scales, from local generation of turbulence to forcing of large-scale circulation (Fritts and Alexander, 2003; Vincent and Alexander, 2020).

This dynamical forcing is most prominent within the mesosphere and lower thermosphere (MLT) at altitudes of typically 50–130 km. Within this range, a large fraction of upward-propagating gravity waves reach their maximum amplitudes and break. The resulting dynamical forcing causes a global-scale circulation within the mesosphere with strong upwelling within the summer polar region and downwelling within the winter polar region (Houghton, 1978; Holton, 1984). Adiabatic cooling and heating connected to this circulation cause thermal conditions within the mesosphere to deviate far away from radiative equilibrium (Solomon et al., 1987; Vargas et al., 2015).

The role of gravity waves is further complicated as they interact with the background flow as they propagate through the atmosphere. This results in an altitude-dependent filtering of the gravity wave spectrum by the background wind, planetary and tidal waves. The gravity wave spectrum reaching higher altitudes thus carries an imprint of the dynamics at lower altitudes. Interactions between gravity waves and the mean flow and subsequent wave breaking then generate secondary waves within the mesosphere that propagate both upward and downward. This happens through the creation of temporally and spatially localized momentum and energy fluxes, which successively create strong local body forces and flow imbalances which then excite the secondary waves (Fritts et al., 2006; Vargas et al., 2016; Vadas et al., 2018; Vadas and Becker, 2018; Becker and Vadas, 2018).

While today the essential nature of the wave-driven circulation of the middle atmosphere is known, important mechanisms and interactions remain to be quantified. Most notably, this concerns wave sources, wave dissipation, and therefore the resulting forcing of the mean flow. A decisive quantity to be specified is the directional F_M, including its altitude dependence and its spectral distribution with reference to horizontal (λ_h) and vertical (λ_z) wavelengths. Ern et al. (2011) have provided global distributions of gravity wave F_M in the mesosphere for the first time using global temperature measurements by the Sounding of the Atmosphere using Broadband Emission Radiometry (SABER). They have shown clearly the dependency of gravity wave F_M deposition according with latitude and longitude (non-uniform longitudinal distribution of flux) at different altitude levels from the stratosphere up to the mesosphere along with their seasonal and longer-term variations. Also, attempts of estimating F_M of small-scale, short-period waves using multiple observation platforms such as aircraft, lidar, airglow sounders, and radars, and satellites have been done (e.g, Suzuki et al., 2010; Bossert et al., 2015), while Gong et al. (2019) and Reichert et al. (2019) have relied on lidar, meteor radar, and SABER data to study a large-scale, long-period waves perturbing the mesosphere temperature and the winds simultaneously. These studies report attempts to characterize the wave field and provide F_M estimations of observed events as well.

To bridge gaps in gravity wave dynamics while estimating their F_M, an observation campaign named SIMONe–2018 (Spread-spectrum Interferometric Multi-static meteor radar Observing Network) was carried from Nov. 2–9 2018, to collect a large number of specular meteor echoes from several locations (e.g., Vierinen et al., 2019; Charuvil et al., 2020). Also, an all-sky airglow imager system running out of the Leibniz Institute of Atmospheric Physics, Kühlungsborn, Germany, was observing the region in parallel to provide image data of the mesosphere and the horizontal structure of atmospheric oscillations during the campaign.

SIMONe–2018 campaign measurements permit to study distinct spatial and temporal scales of gravity waves perturbing the background wind and the airglow simultaneously. In this paper, we have analyzed all-sky imager (ASI) airglow images and multistatic specular meteor radar (MSMR) wind data to access small-scale as well as large-scale gravity wave dynamics using two different analysis methods for each wave category. Airglow images are processed directly using our auto-detection method for small-scale (<725 km), short-period (<1 hour) gravity waves aided by MSMR background wind measurements for Doppler correction of wave apparent periods (τ_o). For nights presenting obvious large-scale (>725 km), long-period (>1 hour) oscillations, wave features are studied via direct examination of large amplitude wind fluctuations and airglow keogram spectral analysis. We have also obtained measurements of the neutral density, temperature, and OH emission volume emission rates from the Sounding of the Atmosphere using Broadband Emission Radiometry (SABER) instrument (Russell et al., 1999; Mlynczak, 1997) aboard the NASA TIMED (Thermosphere, Ionosphere, Mesosphere Energetics and Dynamics) satellite (http://saber.gats-inc.com) to determine the state of the mesosphere region near the observatory during the campaign. This study shows remarkable instances of waves perturbing the airglow and the wind, providing a singular opportunity to examine the linear gravity wave theory's predictions and the occurrence of gravity waves perturbing multiple mesospheric quantities simultaneously. The main contributions here regard the fraction of observed waves carrying substantial F_M with potential to impart significant changes in the 75-110 km dynamics since we show evidences that most observed waves are likely experiencing dissipation in that region.

2 Instrumentation and Data

2.1 All-sky airglow imager (ASI)

An all-sky imager(ASI) assembled at Boston University was deployed in late 2016 at the Leibniz Institute of Atmospheric Physics (IAP) in Kühlungsborn, Germany. The imager is equipped with an Andor back-illuminated bare CCD camera and a 30 mm fish-eye lens which record several nightglow emissions over the entire 180° of the night sky. Andor's iKon-M 934 camera is a 1024 x 1024 array and 13 μm pixel pitch with a 13.3 x 13.3 mm active image area. High sensitivity is achieved through a combination of > 90% QE (back-illuminated sensor), low noise readout electronics, and deep TE cooling down to -60°C. The ASI system uses six interference filters enabling the observation of four mesosphere airglow emissions with a background filter for the hydroxyl emission. A filter for the thermospheric redline (at 630.0 nm) is also available, but images of this emission were not taken during SIMONe–2018 due to filter technical issues. The imaging system operates autonomously via a PC on a nightly basis during moonless periods. Images are obtained on a continuously repeating cycle every ∼2 min with each particular filter accessed every ∼10 min. The specifications of filter wavelengths and integration times are in Table 1. Emission altitudes are discussed in Section 2.3. Preprocessed, low resolution images collected by the ASI are available for visualization at http://sirius.bu.edu/data/. Raw images used in this study are available at https://databank.illinois.edu/datasets/IDB-8585682.

The SIMONe–2018 campaign was carried out for more than a week, but clear skies were seen only during four nights, which limited the optical observations with the all-sky imager. The sky conditions for the four clear nights are summarized in Fig. 1 by zonal and meridional keograms of the O(^{1}S) emission. Appendix C discuss in detail how keograms are built from airglow images. The reader is also referred to Vargas et al. (2020) for more keogram analysis information. Although only keograms of the O(^{1}S) emission are shown here, we have also built keograms for the other three mesospheric emissions, which are available as supplement files of this paper.

The left-hand side panels of Fig. 1 show keograms built directly from O(^{1}S) preprocessed images (Appendix A). The contrast of the images was optimized to show variable features in the brightness present throughout the night. Long-period oscillations seen in the airglow brightness on Nov. 3–4 and Nov. 6–7 keograms indicated by the red ellipses are associated with large-scale, long λ_h gravity waves perturbing the greenline layer. For instance, notice in the meridional keogram of Nov. 3–4 the orientation of the brightness variation associated with a large-scale wave in a region tilted from top to bottom during 1930 UTC to 2230 UTC, indicating a coherent oscillation traveling from north to south. The tilt in the brightness region is not pronounced in the zonal keogram for the same time span, indicating a small, negligible wave component in the west-east direction. Perturbations of the same nature are also seen in the O_2 and OH emissions for the same nights.

The right-hand side panels of Fig. 1 show zonal and meridional keograms built using time-difference (TD) airglow images. Time-difference operation involves subtracting an image from the previous one (same emission) with the goal of filtering out long-term variations in the airglow brightness (e.g., Swenson and Mende, 1994; Swenson and Espy, 1995; Tang et al., 2005; Vargas, 2019). The result is an image where the contrast of shorter-period, smaller-scale (<725 km) oscillations is enhanced. These small-scale waves show up in the keograms as tilted bright/dark bands. Because long-period waves are suppressed, time-difference keograms permit rapid access to the activity of short-period waves each night.

2.2 Multistatic specular meteor radar

During the SIMONe–2018 campaign, MSMR measurements were obtained during seven days continuously. Briefly, the campaign consisted of 14 multistatic links that were obtained by using two pulse transmitters located in Juliusruh (54.63°N, 13.37°E) and Collm (51.31°N, 13.00°E), respectively, and one coded-continuous wave transmitter located in Kühlungsborn. Eight receiving sites were used receiving scattered signal of at least one transmitter. This campaign combines the multistatic approach called MMARIA (Multistatic Multifrequency Agile Radar Investigations of the Atmosphere) (Stober and Chau, 2015) with the SIMONe (Spread Spectrum Interferometric Multistatic meteor radar Observing Network) concept (Chau et al., 2019). In the latter case a combination of spread-spectrum, multiple-input multiple-output, and compressing sensing radar techniques is implemented (Vierinen et al., 2016; Urco et al., 2018, 2019). The winds used in this work have been obtained with a gradient method, i.e., besides the mean horizontal and vertical winds, the gradients of the horizontal components have also been obtained (Chau et al., 2017). Data from one day of this campaign has been used to test a second-order statistics approach by Vierinen et al. (2019). More details of the SIMONe–2018 campaign as well as results of second-order statistics are given in the accompanying paper of this publication (see Charuvil et al., 2020).

Here, we have used the MSMR winds in combination with the airglow data to give a full characterization of the gravity wave dynamics observed during the campaign. Fig. 2 shows the (a) zonal and (b) meridional background winds in the range of 75–105 km measured during SIMONe–2018. Dashed boxes indicate hours of simultaneous operation of the ASI and MSMR systems. The background wind field is calculated from the MSMR measurements using 30-minutes temporal and 1-km spatial windows, respectively. Observe the daily cycle for $z <$80 km and $z >$100 km in the plots that is associated with the variation of meteors detections throughout the day; the meteor density is larger at earlier morning hours and smaller at afternoon hours. Because wind calculation relies on the number of meteors to make quality wind estimations, when not enough meteors are detected, the wind cannot be estimated within a reasonable uncertainty level. The background wind is dominated by a 12-hours tidal oscillation presenting amplitudes larger than 50 ms^{-1}, but spectral analysis reveals the presence of higher tidal harmonics of 8 and 6 hours (see Fig. 6 and Fig. 7).

Fig. 2c and Fig. 2d also presents the zonal and meridional wind fluctuations associated with oscillations caused by gravity waves. To obtain the wind fluctuations, we first average the MSMR raw data over a 400 km^2 field of view using a 4-hour temporal, 4-km vertical windows, respectively. Then, we subtract the result from the background wind field. Notice that oscillations of $\tau_o >$4 hours and $\lambda_z <$4 km will be suppressed, but not completely eliminated in the resulting wind fluctuations. The fluctuation winds show short-period gravity waves perturbing the wind that are also seen in the airglow. For instance, The oscillation evident in the airglow brightness variation (red ellipse) for Nov. 3–4 (Fig. 1c, meridional keogram) is also evident as coherent oscillations in meridional wind fluctuations (red ellipse) on Nov. 3–4 (Fig. 2d).

2.3 Satellite data (TIMED-SABER)

We have also collected observations of the SABER instrument on board the TIMED satellite (Russell et al., 1999; Mlynczak, 1997) within four degrees from the observation site (Fig. 3). The profiles cover the height range from approximately 10 km to more than 100 km. The vertical resolution is ∼2 km. The instrument covers ∼ 52° latitude in one hemisphere to 83° in the other in a given day. The viewing geometry alternates every 60 days due to 180° yaw manoeuvres of the TIMED satellite (Russell et al., 1999). Approximately 1200 temperature profiles are taken each. SABER publications are available at http://saber.gats-inc.com/publications.php.

SABER profiles used here are presented in Fig. 4a–c, while Fig. 4d shows the calculated volume emission rate of the mesosphere airglow emissions as explained below. The thick lines in Fig. 4 indicate the mean of corresponding individual profiles (dotted lines) for the various orbits of the satellite during the campaign. The corresponding orbits are specified in the legend of each chart.

From Fig. 4a, we can verify that the atmosphere is, in average, stable in the altitude range of 88-99 km since the atmosphere lapse rate ($dT/dz =$-3.7 K/km) is larger than the adiabatic lapse rate ($\Gamma =$-9.8 K/km), and is positive ($dT/dz =$1.6 K/km) below and above the 88-99 km range. Even though the satellite orbits registered during SIMONe–2018 were not exactly over the observatory, the instrument measurements are performed in the vertical limb plane that is near or within the field of view of the imager (Fig. 3). Notice that the colored dots indicate where the measurements were made, not the satellite position. Thus, there is a good chance the background atmosphere above the observation site is similar to that indicated by SABER (Fig. 4), although the temperature might still be influenced by gravity waves once we have averaged only a few profiles. Because of that, we are confident using SABER background profiles to make inferences about the propagation conditions for the waves seen over the observatory.

Fig. 4d corresponds to our estimation of volume emission rate (VER) profiles for the OH, O_2, and $O(^1S)$ airglow emissions. These VER profiles were calculated using the mean temperature, atomic oxygen, molecular oxygen, and molecular nitrogen profiles in Fig. 4a–b along with the reaction rates of each emission from Vargas et al. (2007). The characteristics of each layer (measured and calculated VERs) are obtained from a Gaussian model (thin lines in Fig. 4d) to fit each profile from which we obtain the layer peak, width, and the full width at half maximum (FWHM). The mean characteristics of the airglow layers are presented in Table 2. The goodness of fitting scores $R^2 > 0.95$ for all five VER curves. The layer centroids, estimated from

$$z_c = \frac{\int z \, \mathrm{VER} \, dz}{\int \mathrm{VER} \, dz},$$

are in general a few kilometers above the estimated layer peaks because of departures of the actual VER vertical structure from the Gaussian fitting model. We have simulate the VER profile for the OH(8,3) using the SABER mean temperature and atomic oxygen for the campaign. The difference between the simulated OH VER and SABER OH VER lies on the averages used as inputs in the VER simulation. However, SABER OH VER and simulated OH VER are much closer in structure if we use individual SABER temperature and oxygen profiles.

3 Data Analysis and Results

A full characterization of the gravity wave field requires knowledge of the background wind over the observation site. The significant background wind acting in the vicinity of an airglow layer is a function of the vertical structure of the emission (the VER) that has finite thickness (see Fig. 4d). We take that into account by calculating the weighted background wind (Fig. 6a–c) by using the VER of each layer as weighting functions. The weighted wind expression for a given VER is

$$(u_w, v_w) = \frac{\int (u,v) \, \mathrm{VER} \, dz}{\int \mathrm{VER} \, dz},$$

where u_w and v_w are the weighted zonal and meridional winds (Fig. 6), respectively.

3.1 Short-scale gravity wave analysis

We have defined here as small-scale the waves presenting $\lambda_h < 725$ km, while large-scale waves present $\lambda_h > 725$ km. This 725 km threshold corresponds to the length of the diagonal across the field of view of an airglow image mapped into a 512x512 km^2 grid. Thus, a 725 km horizontal scale wave would present one crest and one trough fitting the image frame entirely. More details about raw airglow image preprocessing can be found in Appendix A.

The majority of waves observed during SIMONe–2018 are small-scale, fast oscillations of τ_i <1 hour. The keograms of Fig. 1 (right-hand side panels) show the most prominent waves of this category registered during the clear nights of the campaign. These short-scale gravity waves are analysed here using the auto-detection method (Tang et al., 2005; Vargas et al., 2009; Vargas, 2019). Further details about the method is found in Appendix B.

Fig. 5 shows the results from the auto-detection method for all the emissions recorded during SIMONe–2018. Weighted background winds in Fig. 6a–c were used to carry out the Doppler shift correction on τ_o. Thus, the parameters shown correspond to intrinsic properties of the waves. We have calculated the error bars for the parameters of each wave event measured using the methodology in Vargas et al. (2019). The average error of each parameter is shown in their respective charts in Fig. 5. Since we rely on a set of three images at the time to compute the cross-spectrogram of a set. The time span of each set is about 30 minutes and most of waves would have completely disappeared the imager field of view (FOV) within that time because the duration of a gravity wave is generally short. Thus, is more likely that the observed wave events represent waves independent from one another.

Because every image of a given airglow layer is taken at 10 minutes pace (the filter wheel cycle period), we are only able to resolve wave apparent periods >20 minutes. On the other hand, the exposure time used here is mostly 2 minutes, aliasing could be present due to this relatively long exposure time. However, we have assured the aliasing is minimal in this case because there is no smudging of the small-scale wave structures seen in the images.

The top-center box (Fig. 5c) contains a statistics summary of the measured wave parameters . Fig. 5j shows λ_z ranging from 10 to 40 km, while λ_h in Fig. 5m clusters around 75–125 km. Waves transporting large F_M are mainly oriented towards Northwest and Southwest (Fig. 5a), but the polar histogram in Fig. 5f shows a large number of waves traveling southeastward into the dominant wind orientation (Fig. 5k). Estimated τ_i shown in Fig. 5e range within 20–40 minutes, with intrinsic phase speeds in the interval of 30-100 ms^{-1} in the campaign (Fig. 5b). The largest wave relative amplitude estimated from the images is 7% in Fig. 5d, but this does not necessarily translate into large F_M waves, which depends on other wave parameters.

Since the auto-detection method return wave intrinsic parameters, we are able to estimate F_M of every measured event (e.g., Vargas et al., 2007). Fig. 5l shows the daily F_M of waves detected during SIMONe–2018, with larger F_M waves appearing on Nov. 2–3 and Nov. 3–4. The momentum flux vs. intrinsic wave period chart (Fig. 5g) reveals a tendency of larger τ_i waves carrying larger F_M. Conversely, Fig. 5h (Fig. 5i) reveals that large λ_h (λ_z) waves associate with small F_M quantities.

3.2 Large-scale gravity wave analysis

During SIMONe–2018, we have also observed the presence of large-scale gravity waves modulating simultaneously the airglow brightness (Fig. 1c and Fig. 1e) and the horizontal wind (Fig. 2c and Fig. 2d). To study these large-scale oscillations in the wind at the altitude of the airglow, we have calculated the wind fluctuations weighted by the volume emission rate of each layer using

$$(u'_w, v'_w) = \frac{\int (u', v')\,\mathrm{VER}\,dz}{\int \mathrm{VER}\,dz}$$

The result is seen in Fig. 6d–f, where the dashed boxes indicate hours of simultaneous operation of the ASI and MSMR systems.

The weighted wind fluctuations are similar in each layer once the layers peak within ±2 km from each other (see Table 2) and are thicker (mean FWHM∼15 km) than expected (e.g., Greer et al., 1986; Gobbi et al., 1992; Melo et al., 1996; Wüst et al., 2017). The similarity of these fluctuations is related to long λ_z waves seen in Fig. 2c and Fig. 2d. Moreover, because the overlap of the VER profiles is non-negligible, the rms values of the weighted winds fluctuations are expected to have similar magnitude. Calculated rms magnitudes are 6.9±1.0 ms^{-1} and 5.9±0.9 ms^{-1} in the zonal and meridional directions, respectively.

The spectral content of the weighted wind fluctuations is shown in Fig. 7. Several tidal harmonics are still present in the spectra (vertical dotted red lines in Fig. 7). This is due to how the wind fluctuations are calculated, i.e., by first using a 4-hour temporal, 4-km vertical windows to obtain winds representing scales larger, then subtracting the result from the background wind. Thus, the obtained wind fluctuations will contain some of the energy of the tidal modes. However, there are persisting peaks attributed to gravity waves because of their presence in wind fluctuations and keograms. For instance, the peaks in Fig. 7 at the vicinity of 0.24 cycles/hour are seen in the wind fluctuation of Nov. 3–4 (meridional direction). Likewise, Fig. 7 shows a peak near 0.11 cycles/hour corresponding to a wave of 8.9±1.0 hours also seen in the keograms of Nov. 6–7 (zonal direction). A hodograph analysis of the winds must be carried out in a separate work to clarify the nature of the significant peaks in Fig. 7.

We have studied further the wind fluctuations against obvious wave features present in the keograms of Nov. 3–4 and Nov. 6–7. By visual inspection of the images, we have verified that these large-scale waves do not fit within the airglow image field of view (512x512 km^2) and are only noticeable via keogram analysis. We carry out the analysis by overlapping the $O(^1S)$ weighted wind fluctuations on top of the corresponding keograms for these nights (Fig. 8).

On Nov. 3–4 (Fig. 8a), a strong and coherent oscillation is observed in the meridional wind fluctuation while both zonal and meridional keograms present enhanced brightness structures around 2100 UTC (dashed black lines). As the meridional wind fluctuation peaks, the meridional keogram brightness dims (Fig. 8a bottom); as the meridional wind fluctuation reverses direction, the airglow brightens. We have estimated $\tau_o \sim 4.0\pm1.0$ hours for this oscillation from the meridional wind fluctuations, where the assigned uncertainty in τ_o corresponds to the smallest division in the keogram temporal axis. The tilted brightness structure between 1900 and 2100 UTC in the meridional keogram indicates a wave is traveling southwards. The zonal keogram shows no obvious tilt in the enhanced brightness, suggesting no wave propagation in the east-west direction. That is confirmed from zonal wind (Fig. 8a top) that does not show any apparent oscillation in the same time span.

Similarly, we have observed enhancements in the airglow brightness on Nov. 6–7 associated with a large-scale wave with $\tau_o \sim 8.0\pm1.0$ hours estimated from the wave activity in the zonal wind fluctuation seen in Fig. 8b top. The zonal wind fluctuation coincides well with the $O(^1S)$ enhanced brightness structure in the zonal keogram around 0000 UTC. This brightness enhancement shows a slight tilt that indicates a wave propagating from west to east. The negligible brightness tilt in the meridional keogram (Fig. 8b bottom) implies the wave has no evident north-south component.

Spectral analysis of keograms for the two nights showing large-scale waves is in Fig. 9. The zonal and meridional keogram spectra for Nov. 3–4 are in Fig. 9a and Fig. 9c, while zonal and meridional keogram spectra for Nov. 6–7 are in Fig. 9b and Fig. 9d. Appendix C gives further details about the keogram spectral analysis carried out here.

For Nov. 3-4, the zonal keogram spectrum indicates a peak at $k_x = 0$ and $\omega_o = -0.17$ cycles/hour (τ_o =5.7±1.0 hours), where the negative sign is associated with a forward evolving time. The meridional keogram spectrum shows a dominant peak at $\omega_o = -0.21$ cycles/hour (τ_o =4.6±1.0 hours) and $k_y \sim -0.7 \times 10^{-3}$ cycles/km (λ_y ∼1365±136 km), where the negative sign indicates a southward-propagating wave. The error in λ_y is based on Vargas (2019) that estimates 10% error in measurements of large horizontal scale waves (> 100 km) from spectral analysis. Notice that because the horizontal scale of the wave in the meridional direction is twice as large as the mapped image FOV (512x512 km^2), the entire horizontal wave structure is hardly seen in a single airglow image, but is doubtless recognized in the keogram.

The large-scale wave occurring on Nov 6–7 is represented in the zonal spectrum by the peak near $\omega_o \sim -0.11$ cycles/hour (τ_o =9.1±1.0 hours) and $k_x \sim 0.2 \times 10^{-3}$ cycles/km (λ_x ∼4096±409 km), where the positive sign indicates an eastward-propagating wave. The meridional keogram spectrum indicates a peak at the same frequency but $k_y \sim 0$, indicating no wave propagation in the meridional direction.

Fig. 10 shows the time-altitude cross-section of the zonal and meridional wind fluctuations for the nights of Nov. 3–4 and Nov. 6–7, respectively. The descending phase progression in time-altitude cross-section revels these large-scale waves are propagating upwards. We have drawn continuous (dotted) white lines on top of the crests (troughs) of the salient wave structures to estimate λ_z and τ_o of the oscillations. The lines were drawn where the wave structures are better defined on top of the meridional wind (Nov. 3–4) and zonal wind (Nov. 6–7) fluctuation cross-sections. From these lines, we have estimated λ_z =25.6±1.0 km and τ_o =4.3±1.0 hours for the wave seen on Nov. 3–4. Notice the assigned error of 1 km in λ_z corresponds to ∼2 times the the vertical resolution of the vertical axis in Fig. 10, while the assigned error of 1 hour in τ_o corresponds to the resolution of the temporal axis in Fig. 10.

For the wave seen in Nov. 6–7 we have obtained τ_o =8.0±1.0 hours and λ_z =21.3±1.0 km. This long-period wave is not related to the 8-hour tide since the horizontal structure of the oscillation can be seen in the keogram of Fig. 8b entirely. The apparent periods derived here from the descending phase analysis are consistent with those from the keogram spectral analysis shown earlier.

4 Discussion

The propagation conditions for gravity waves during SIMONe–2018 are depicted in Fig. 4 showing the temperature and constituent densities near the Kühlungsborn observatory. While the vertical structures of the atomic oxygen density appear normal, the mean temperature indicates convectively favorable conditions for gravity wave vertical propagation as the ambient lapse rate is positive for $z >\sim 87$ km and $z <\sim 99$ km. Within 86–98 km range, the ambient lapse rate is negative but still sub-adiabatic, and convective instabilities are unlikely to form under these conditions. Thus, gravity wave dissipation due to convective instabilities would not affect the vertical evolution of the gravity wave field during the campaign. We have also verified that dynamic instabilities did not occur because the wind shear was <30 ms^{-1}/km most of the time during the campaign. On the other hand, because the horizontal winds occasionally achieved relatively large magnitudes >50 ms^{-1} (Fig. 2a and Fig. 2b), the wind field could have caused absorption of waves having phase speed <50 ms^{-1} traveling to the same direction of the background wind.

We can verify the effect of background wind on the propagation direction of the waves by examining Fig. 5. The momentum flux vs. propagation direction chart (Fig. 5a) shows a number of waves with large F_M oriented towards northwest and southwest, while Fig. 5k shows a dominant southeastward wind during SIMONe–2018 observations. Thus, it is likely that the background wind controls the propagation of southeastward waves via dynamic filtering. However, the wave propagation direction histogram (Fig. 5f) indicates that a significant number of waves still propagate into the wind. These waves must then have horizontal phase speed larger than the background wind. In fact, we have estimated an average c_i =56.6±13.6 ms^{-1} for waves traveling in the southeast quadrant sector (270° to 360°), while wind has mean magnitude of 39.3±18.9 ms^{-1} in the same sector (Fig. 5k. This suggests these fast waves were able to overcome absorption levels while propagating vertically.

Horizontal and vertical wavelengths, intrinsic periods, and intrinsic phase speeds of waves detected during SIMONe–2018 are directly comparable with the results of Li et al. (2011), which used a similar auto-detection method to analyze short-period, fast gravity waves in the airglow. Our statistics show an average λ_z of 18.5±4.6 km (4.6 km is the sample standard deviation), which is compatible with the results of Li et al. (2011) showing λ_z clustering from 20 to 30 km. They have shown λ_h clustering around 15–30 km, while our results peak around 75–100 km. Fast waves reported here present remarkably larger horizontal scales than those of Li et al. (2011), which could be associated with the location and type of terrain (Maui–sea vs. Kühlungsborn–land) and gravity wave sources acting near the observatories. Yet, our sample is representative of the winter solstice conditions observed for a week, while that from Maui is representative of the season conditions observed over five years.

There are obvious discrepancies in τ_i estimated here against those of Li et al. (2011). Observe that τ_i here bulks around 20 to 30 minutes, while Li et al. (2011) report 77% of waves having τ_i <10 minutes. We attribute this discrepancy to the different integration time and the filter wheel cycle of the observing airglow camera systems; during SIMONe–2018, we have observed several emissions using a filter wheel cycle period of 10 minutes, which allows us to detect waves presenting τ_o >20 minutes. Li et al. (2011) used a filter wheel cycle of 2 minutes while observing a single emission, allowing detection of waves of time scales as short as ∼5–6 minutes near the Brunt-Väisälä period. The filter wheel cycle time seems to affect other parameters as well. For instance, while Li et al. (2011) report a majority of wave intrinsic phase speeds in the range of 50–100 ms^{-1}; we have estimated slower intrinsic phase speeds of 31.2±17.3 ms^{-1}. The filter wheel cycle influences the sensitivity of the measurement system in the temporal domain, but not the spatial domain, that is, the system will automatically detect faster waves having smaller-periods but in the same λ_h range.

In another study, Li (2011) used one year of OH airglow observations over the Andes Lidar Observatory (ALO) in South America to characterize small-scale, fast gravity waves. He found that the peak of distribution of λ_h falls in the 20–30 km range, c_i ranges mainly 40–100 ms^{-1} (peak at 70 ms^{-1}), 80% of the τ_i population ranges from 5–20 minutes, and λ_z distribution peaks around 15 km. These results resemble those of Maui, and the same discrepancies from the results in SIMONe–2018 are applicable. However, the sources of waves over the South American observatory are much clearer and related with convection in central Argentina to the east of ALO. These sources generate fast, short-period, small horizontal scale waves that can be captured over the ALO imager. The farther away the source, the fewer short-periods waves are seen, which explains a secondary peak around λ_h =80–100 km shown in Li (2011). This range is comparable to the λ_h distribution from the SIMONe–2018 campaign showing a peak around λ_h =75–100 km that would be related with tropospheric convective sources active to the north and east of Kühlungsborn during SIMONe–2018.

The momentum flux of high-frequency waves detected during SIMONe–2018 (Fig. 5) is calculated using Vargas et al. (2007, Eq. 13) as showed in Appendix B. The mean momentum flux has a larger component towards the west of -0.36±1.51 m^2s^{-2}. Notice the mean F_M shows tendency of a net wave motion westward, while the standard deviation indicates that waves could be moving westward or eastward. The F_M meridional component is ∼1/6 of the zonal magnitude. Ignoring for a moment the wave propagation direction, the mean F_M =1.62±2.70 m^2s^{-2}. For all the 362 waves detected during SIMONe–2018, 50% of the total F_M is due to waves carrying F_M >3 m^2s^{-2} (40 events), that is, only 11% of the detected waves are responsible for 50% of F_M measured during the campaign. This result agrees with the findings of Cao and Liu (2016) that show most of F_M is due to waves that occur very infrequently (low intermittency). However, Cao and Liu (2016) also conclude that small F_M waves are important because of their higher occurrence rate.

Observe that not necessarily the 362 detected events are independent, that is, the same wave could have been detected multiple times throughout the night. However, we rely on sets of three images to make wave detections. Since the time span of each set is about 30 minutes (10 minutes between successive images), waves detected in the given set would have disappeared from the imager FOV after that time span. This is because the duration of quasi-monochromatic wave packets in airglow images are generally short. Thus, the same waves are unlike be detected in multiple image sets. This way, it would be more likely that most of the 362 detections correspond to different, independent waves.

In spite of the small mean value, F_M bursts between 10–30 m^2s^{-2} were mainly seen in the O_2 emission during the campaign. These waves were traveling northwestward with τ_i =30–40 minutes, λ_h ∼90 km, and λ_z =12–15 km (see charts of each emission in the supplement files of this publication). The sum of F_M of these waves (8 events) accounts for 20% of the total small-scale wave F_M measured during the campaign. It is not clear why the enhanced waves are seen most in the O_2 emission once the layer's peaks nearly overlap, but could be related to that the O_2 VER having a narrower FWHM (see Table 2). This way, shorter λ_z waves would be detected primarily in O_2 images, presenting larger F_M since it increases as λ_z decreases (Fig. 5i).

We see that even in smaller numbers, the more energetic, larger F_M waves could have greater impact in the atmosphere. For instance, Bossert et al. (2015) investigated, during the Deep Propagating Gravity Wave Experiment (DEEPWAVE), mountain waves presenting horizontal scales of 200–300 km with F_M in the range of 20-105 m^2s^{-2}. Similarly, Smith et al. (2020) estimated F_M ∼232 m^2s^{-2} associated with an extensive and bright mesospheric gravity wave event seen over the El Leoncito Observatory, Argentina (31.8° S, 69.3° W), during the nights of 17 and 18 March 2016. The waves observed in this study carrying F_M >3 m^2s^{-2} would potentially cause F_D ∼ 22–41 ms^{-1}/day (Vargas et al., 2007, Fig. 9e), considering that the wave breaking continues for 24 hours. This would lead to considerable mean flow deceleration and body forces capable of exciting secondary waves as point-like sources (Vadas and Becker, 2018). Considering the wave source and wave breaking mechanism acting for 4 hours (about half of a typical nighttime observation period) in a given altitude, we estimate a potential mean flow deceleration of 3.7–6.8 ms^{-1} in this time span (4 hours) due to wave forcing.

In a similar study, Suzuki et al. (2010) demonstrate identical gravity wave structure detected in airglow intensity, radar wind, and lidar temperature. In airglow keograms from northern hemisphere stations in Japan, they observed small-scale gravity waves with $\lambda_h \sim$170 km, period of 1 hour propagating northeastward at $\sim$50 ms^{-1}. Using from both airglow images and meteor radar wind, they have demonstrated an average F_M of 0.8 m^2s^{-2} at 94 km and 1.5 m^2s^{-2} at 86 km for the observed oscillations. The Suzuki et al. (2010) flux measurements agree with our estimates for small-scale waves that show a majority of events carrying small F_M. They have also estimated the acceleration of 0.8 ms^{-1}/hour (19.2 ms^{-1}/day) at the 94 km height, which is close to our estimations of F_D for small-scale waves.

Ern et al. (2011) shows absolute F_M values of $\sim 10^{-3.9}$ Pa at 50 km altitude and $\sim 10^{-4.3}$ Pa at 70 km altitude in the northern hemisphere in January for latitudes/longitudes near the Kühlungsborn observatory, evidencing momentum flux deposition in the middle atmosphere. Thus, it is likely that small-scale waves observed here are mostly dissipating as they travel through the MLT, in agreement with Vargas et al. (2019). In other flux estimation study using airglow imagery of gravity waves, Vargas et al. (2009) has reveled F_M ranging from $\sim$1.5 to $\sim$4.5 m^2/s^2, while radar measurements of (e.g, Yuan and Fritts, 1989) estimated F_M =5–15 m^2/s^2. Also, it is believed 70% of the momentum is carried by short-period waves (<1 hour) (Vincent, 1984). Estimations of F_D (wave drag) in the meridional direction from airglow measurements unveiled accelerations of 3 ms^{-1}/day (Vargas et al., 2015), which is significant given that the meridional wind magnitude is weak ($\sim$20 ms^{-1} or less at mid latitudes), while in the zonal wind the wave F_D =15–60 ms^{-1}/day (Vincent and Fritts, 1987).

We have also estimated the horizontal wavenumber and apparent frequency of the large-scale waves shown in the airglow (Fig. 8) from the spectrum of the zonal and meridional keograms in Fig. 9. We then estimate λ_z of the events assuming a Brunt-Väisälä period of 5.5 minutes ($N = 0.01904$ rad/sec) and an inertial period of 14.8 hours ($f = 0.11816 \times 10^{-3}$ rad/sec) for the Kühlungsborn latitude. We use the acceleration due to gravity $g = 9.5$ m/s^{-2} for the mesosphere.

The wave occurring on Nov. 3–4 presents $k_h = k_y = -0.7 \times 10^{-3}$ cycles/km and $\omega_o = 0.215$ cycles/hour estimated from the keogram spectra. Weighted background wind field over the observatory at 2315 UTC presented $u = 28.5$ ms^{-1} and $v = -1.4$ ms^{-1} at the instant the wave was in the dimmer phase of its cycle in the airglow. Applying then Doppler shift correction, we estimate an intrinsic frequency $\omega = 0.211$ cycles/hour for the wave. Finally, using the dispersion relation (Appendix C), we derive $\lambda_z = 25.1 \pm 2.5$ km for the Nov. 3–4 wave, where the uncertainty is 20% as estimated in Vargas (2019). This wavelength compares well with $\lambda_z = 25.6 \pm 1.0$ km obtained by visual inspection of Fig. 10.

Likewise, the Nov. 6–7 wave has $k_h = k_x \sim 0.2441 \times 10^{-3}$ cycles/km and $\omega_o = 0.11$ cycles/hour. Applying once again the Doppler shift correction using background wind components of $u = 26.0$ ms^{-1} and $v = -30.0$ ms^{-1} at 2326 UTC, we obtain an intrinsic frequency of $\omega = 0.087$ cycles/hour. From the dispersion relation we then estimate $\lambda_z = 20.5 \pm 2.0$ km for this wave, which also agrees with the measured value of $\lambda_z = 21.3 \pm 1.0$ km from Fig. 10.

The amplitude of the large-scale from keogram waves are $I'_{\%}$ =36.5% (Nov. 3–4 @ 2130 UTC) and $I'_{\%}$ =47.9% (Nov. 6–7 @ 0030 UTC). These amplitudes are relative to the mean airglow brightness of each night. As demonstrated in Appendix B, the vertical wavelength of each wave along with their perturbations in brightness permit to evaluate their relative perturbation in temperature as $T'_{\%}$ =9.1% (Nov. 3–4) and $T'_{\%}$ =13.7% (Nov. 3–4). Then, we finally estimate F_M (see Appendix B) by using the intrinsic parameters found for the observed large-scale waves, which are $F_M = 21.2\ \mathrm{m}^2\mathrm{s}^{-2}$ for the wave seen on Nov. 3–4, and $F_M = 29.6\ \mathrm{m}^2\mathrm{s}^{-2}$ for that seen on Nov. 6–7. Table 3 shows a summary of the main features of the large-scale waves as discussed above. We expect the uncertainties in F_M to be large (>40%) given that the F_M variables incur in uncertainties that are transferred to F_M via error propagation (Vargas, 2019).

Based upon F_M values of the large-scale waves, we estimate for the southward-traveling wave (Nov. 3–4) a momentum flux divergence F_D ~43 ms^{-1}/day in the meridional flow, assuming this wave breaks or dissipates in a given level along its vertical path. Similarly, the Nov. 6–7 wave would cause a deceleration of F_D ~38 ms^{-1}/day in the zonal flow in the breaking or dissipation level. These large-scale, large amplitudes waves would have a greater impact on the mean flow than small-scale waves, even though these waves are less frequent in mesospheric measurements than their small-scale counterparts.

Gong et al. (2019) has also investigate the properties of large-scale, long-period waves observed on May 30, 2012 in China. Datasets of three instruments used in the study have shown evidences of a same gravity wave perturbing lidar and SABER temperatures as well as meteor radar winds. The parameters associated with the observed wave are λ_h =560 km, λ_z =8–10 km, τ_o = 6.6–7.4 hours, and phase speed of 21 ms^{-1}. Gong et al. (2019) and Reichert et al. (2019) along with our study represent few efforts to characterize larger-scale gravity waves propagating from the stratosphere into the mesosphere using multi-instrument datasets.

According to Vargas et al. (2019), only a minority of waves seen in the airglow(~5%) are in non-dissipating regime. Vargas et al. (2019) also shows that the majority of the gravity waves present strong dissipation and transfer momentum flux to the main flow within a distance of two atmosphere scale heights (12-14 km). Thus, large F_M waves discussed here are likely to present dissipative or breaking characteristics given their larger amplitudes. This is not without controversy, since recent radar measurements in Antartica (Sato et al., 2017) have shown longer-period gravity waves (1 hour–1 day) transporting larger F_M, although short-period oscillations also have significant F_M but relatively smaller.

Recently, Vadas and Becker (2018) have modeled the evolution of mountain waves over the Antarctic Peninsula after observational results of large-scale, long-period waves seen in the mesosphere (Chen et al., 2013, 2016) attributed to an unbalanced flow in the lower stratosphere. This imbalance excited upward (downward) propagating oscillations from the knee of fishbone-like structures at 40 km altitude, which are associated with the excitation of secondary waves from the breaking of extensive mountain wave structures. Although other modeling efforts also attribute the excitation of non-primary waves to localized turbulence eddies from gravity wave breaking (e.g., Heale et al., 2020), we believe that the large-scale waves observed in this study are the product of the Vadas and Becker (2018) mechanism at play in the stratosphere. In fact, preliminary analysis of temperature profiles at 0–90 km altitude acquired by the IAP Rayleigh Lidar system on Nov. 6–7 revealed fishbone structures at 40-45 km, resembling the predictions of Vadas and Becker (2018). We will investigate in detail the possible connection with the large-scale waves seen here in a separate paper; specifically, we want to identify potential sources of primary waves in the vicinity of Kühlungsborn during SIMONe–2018, and also trace the observed large-scale waves back to their excitation altitude around the fishbone knee region at 40-45 km revealed in the filtered lidar temperatures.

5 Conclusions

In this paper, gravity waves of small and large horizontal scales were characterized by their intrinsic wave parameters, amplitudes, momentum fluxes, and momentum flux divergences. We have focused the analysis on data recorded simultaneously by an airglow all-sky camera, multistatic specular meteor radar, and TIMED/SABER satellite to obtain a more extensive collection of complementary information about the state of the mesosphere region over the observatory during the campaign. To uncover small horizontal scale features, we have used an auto-detection method to process all-sky airglow images and background meteor radar winds. Large-scale waves were characterized by spectral analysis of airglow keograms and altitude vs. time cross-section of wind fluctuations.

Our results indicate that 11% of all detected gravity wave events have large amplitudes and carry 50% of the total F_M estimated during SIMONe–2018. These fewer wave events could impart mean flow deceleration of F_D =21–43 ms^{-1}/day towards the wave propagation direction at breaking or dissipation levels. We have estimated F_D using Vargas et al. (2007, Fig. 9e) results for waves having $\lambda_z = $ 20–25 km and $\lambda_z >$100 km. However, the deceleration will be much less because the waves are unlike to be breaking or dissipating continuously for 24 hours, dying out earlier.

Given the relatively large λ_z and λ_h of the observed large-scale waves, there is a possibility that these events are the product of secondary wave excitation via the mechanism identified by Vadas and Becker (2018). This possibility is supported by stratosphere fishbone structures uncovered in filtered temperatures collected over Kühlungsborn with the IAP Rayleigh Lidar system on Nov. 6–7. A complete analysis of these structures will be given in a separate paper, in which we also plan to show the origin of the primary waves in the troposphere from weather images as well as the presence of non-primary waves in other datasets such as that of the AIRS on board the AQUA satellite.

Appendix A: Airglow Image Preprocessing

For a given observation night, in the absence of contamination sources (e.g., cloudiness), a series of airglow images is produced by our airglow imager system with 10 minutes per image and ∼2 minutes integration time. Prior to carry out spectral analysis, each raw airglow image must pass through a series of preprocessing steps. First, the image frame is centralized such as the image zenith coincides with the central pixel of the image frame. Second, the image is rotated and flipped over such as the image top points northward and the image left points eastward. Third, the stars are removed using a star suppression algorithm Tang et al. (2005). Forth, the resulting image is then mapped onto a geographic plane of 512x512 km^2 projected at the height of the emission layer Garcia et al. (1997). Fifth, the images are detrended by subtracting a fitted linear surface from the image frame. After these preprocessing steps, the resulting frames are then uniform across the FOV with a pixel resolution of 1 km/pixel and ready for spectral analysis (auto-detection or keogram spectral analysis methods) to obtain gravity wave parameters present in the images.

Appendix B: Auto-Detection Method

The auto-detection method for image processing and analysis was used in this study to obtain parameters of quasi-monochromatic waves from sequences of airglow images. This process detects waves and estimates its parameters automatically, making the study of gravity waves more effective, especially in relation to the estimation of F_M. Compared to conventional techniques, which involve looking for waves from visual inspection of preprocessed image sequences. This method is more optimized because it processes a set of three images at a time, requiring relatively less processing time.

The F_M carried by vertically propagating waves are estimated from intrinsic parameters waves, knowing the prevailing wind calculated from meteoric radar data. Preprocessed images mapped in a 512x512 km^2 grid are cropped around the zenith to produce the 174x174 km^2 analysis window because the central region of the image is less sensitive to lens distortion.

The method corrects automatically τ_o Doppler shift due to the background wind. This is done by shifting the image pixels of each direction by a distance proportional to the wind velocity divided by the image acquisition period (Tang et al., 2005). Pixel shifting is performed in the first and last images of a set. The corrected set are used to compose two TD images. A TD image is produced by subtracting an image from the previous one in the image set (Swenson and Mende, 1994; Swenson and Espy, 1995; Tang et al., 2005; Vargas, 2019).

Two TD images are generated from sets of three consecutive preprocessed airglow images around a given instant. The Fourier transform is applied to each TD image, and the cross-spectrum is then obtained from the individual TD spectra. Thus, the spectrograms of each TD image are obtained from the 2D-FFT transform, which, in turn, are combined to form the cross-spectrogram of the image set (e.g., Vargas, 2019).

Let $J_1(k_x, k_y)$ and $J_2(k_x, k_y)$ be the Fourier transforms of two TD images from a given set. In general, lateral lobes associated with spectral peaks appear in the spectrogram as a result of the limited spatial extent of the image. In this work, we applied the 2D Hanning window in the TD images to minimize the lateral lobes while preserving the energy of sinusoidal components associated with gravity waves. The cross-spectrogram is described in terms of both $J_1(k_x, k_y)$ and $J_2(k_x, k_y)$ as

$$I_{1,2} = \frac{J_1(k_x, k_y) J_2^*(k_x, k_y)}{n^2}$$

where the asterisk designates the complex conjugate and n^2 the number of pixels in the image. The cross-spectrogram contains information about the wavenumber, temporal frequencies, and the phase difference of the dominant components of the spectrum.

The dominant wavenumbers of the image set are then identified from the amplitude cross-spectrogram $|I_{1,2}|$, while the dominant wave periods are determined from the phase cross-spectrogram. The wavenumbers k_x and k_y are determined at the location of the ith spectral peak to obtain $\mathbf{k_h} = (k_x, k_y)$, providing $\lambda_h = 1/(k_x^2 + k_y^2)^{\frac{1}{2}}$. The wave orientation is then $\phi = \tan^{-1}(\frac{k_y}{k_x})$.

From the phase cross-spectrogram we obtain the phase shift $\delta\theta$ of the wave between TD images at the location of the spectral peak (k_x,k_y). We now can estimate the c_i of the wave using

$$c_i = \frac{1}{2\pi} \frac{\delta\theta}{\delta t} \lambda_h,$$

where δt =10 minutes the filter wheel cycle period. The intrinsic wave period is then found from $\tau_i = \frac{2\pi}{\omega} = \frac{\lambda_h}{c_i}$. Notice that at this point, the wave propagation direction ϕ has an 180° ambiguity. This ambiguity is resolved by taking the (k_x,k_y) pair values from the phase cross-spectrogram where $\delta\theta < 0$, which corresponds to a time coordinate progressing forward.

The airglow brightness I detected by the CCD sensor can be considered as the superposition of a basic state $\bar{I}$ and a state disturbed by waves I' such as $I = \bar{I} + I'$. Again, I' is estimated in the wavenumber domain based on the amplitude cross-spectrogram. The undisturbed component $\bar{I}$, on the other hand, is obtained by the mean airglow brightness over the image field of view.

The relative wave amplitude in intensity $I'_{\%} = 100 \times (\frac{I'}{\bar{I}})$ over the FOV is estimated by integrating the energy around a given spectral peak. The wave information is only stored if $I'_{\%}$ has energy >10% of the total cross-spectrogram energy. The basic hypothesis for restoring the wave energy is that the wave content throughout the image is uniform. However, the animation of TD images reveals that monochromatic waves do not always cover the entire FOV, thus, the energy extracted from the wavenumber domain represents an average wave energy over the FOV. The size of the analysis window (174x174 km^2) is important because it is small enough to allow the wave event cover the entire FOV, giving a more accurate estimate of its energy, and large enough to ensure the detection of waves in the range of 2–174 km. Notice that while this procedure restricts the field of view, dynamic parameters of gravity waves can be estimated more reliably since the full wave structure is captured by this smaller analysis window.

We then evaluate $\lambda_z = \frac{2\pi}{m}$ using the complete gravity wave dispersion relation

$$m^2 = \frac{(N^2 - \omega^2)}{(\omega^2 - f^2)} k_h^2 + \frac{\omega^2}{\gamma g H} - \frac{1}{4H^2}$$

where $\gamma = c_p/cv$ the ratio of specific heats and H the scale height in the MLT, while g, and N are the acceleration due to gravity and the Brunt-Väisälä frequency, respectively.

The momentum flux is calculated using Vargas et al. (2007, Eq. 13)

$$F_M = -\frac{1}{2}\frac{\omega^2 g^2 m}{N^4 k_h} |\frac{T'_{\%}}{100}|^2,$$

where ω, k_h, m, $T'_{\%}$, g, and N are the wave angular intrinsic frequency, horizontal wavenumber, vertical wavenumber, percent temperature fluctuation, acceleration due to gravity, and the Brunt-Väisälä frequency, respectively. The percent temperature fluctuation $T'_{\%}$ is calculated using the cancellation factor Vargas et al. (2007, Eq. 12)

$$CF = \frac{I'_{\%}}{T'_{\%}} = 4.6 - 3.7e^{0.006(\lambda_z - 6)},$$

as the relative wave amplitude in intensity $I'_{\%}$ is obtained from the amplitude spectrogram as described earlier.

The operations above run in a loop that iterates continuously for the the number of images collected in a given observation night. The wave parameters, their uncertainties, and the occurrence time stamps of the events are stored in a separated file for each night.

Appendix C: Keogram Spectral Analysis

While individual airglow images represent a routine way to study short-period, small-scale gravity waves, keograms are conveniently used in this study to investigate the characteristics of major low-frequency, large-scale oscillations, revealing wave activity over the time span of the observation night.

We built zonal (meridional) keogram by taking the central row (column) of raw or preprocessed airglow images collected in a given observation night (Vargas et al., 2020). In the zonal keogram, the vertical scale indicates west (negative) and east (positive), while the vertical scale in meridional keograms indicates south (negative) and north (positive). The horizontal scale in both zonal and meridional keograms refers to the universal coordinated time (UT). Notice the center of vertical axis of the keograms corresponds to the brightness registered by the zenith pixel localized at the center of the images.

Large and small scale waves show up in keograms as tilted luminous or dark patches. The deeper the tilt is, the slower the phase speed (long τ_o) of the wave (Vargas et al., 2020). The horizontal wavelength can be also determined from keogram images as long the wave has nonzero phase speed at least in a given direction (zonal or meridional). The wave tilt angle is measured from the horizontal axis to the wave luminous patch in the keogram, and is positive if the wave travels eastward (northward) in the zonal (meridional) keogram.

Zonal and meridional keograms are airglow brightness time series as a function of zonal and meridional distances. The temporal axis has resolution of 10 minutes and the spatial axis (zonal and meridional) have resolution of 1 km/pixel. Thus, waves presenting τ_o >20 minutes and λ_h >2 km can be resolved by this method. The spectral analysis of keograms is carried out in the Fourier space via 2D-FFT preceded by Hanning windowing. The spectral content of the zonal (meridional) keogram can be seen in Fig. 9a (Fig. 9c). To obtain the wave parameters from the keogram spectrum, the wavenumbers of higher energy are selected in the range of $\omega_o < 0$ only, which corresponds to time progressing forward. Notice that by considering $\omega_o < 0$, the ambiguity in the wave propagation direction is resolved.

The ith spectral peak in the spectrogram are pairs (k_x,ω_o) and (k_y,ω_o) from the zonal and meridional keograms spectrum, respectively. These pairs correspond to parameters of prominent large-scale waves seen in the keograms. Here, k_x, k_y are the zonal and meridional wavenumber components of $\mathbf{k_h} = (k_x, k_y)$ from where we obtain $\lambda_h = 1/(k_x^2 + k_y^2)^{\frac{1}{2}}$. The apparent wave frequency is ω_o, from where we obtain the apparent wave period $\tau_o = 1/\omega_o$. Notice that τ_o can be determined from both zonal or meridional keogram spectrum since the temporal axis is common to both of them.

The intrinsic frequency ω is determined using background winds from meteor radar projected in the direction of wave propagation. This dependency is described by $\omega = \frac{2\pi}{\tau_o} - \mathbf{k_h}\cdot\mathbf{v}$, where $\mathbf{v} = (u,v)$, u and v are the background wind components in the zonal and meridional directions, respectively.

We can combine the observed frequency with the observed background wind to derive τ_i of the waves using $\omega = \omega_o - \mathbf{k_h}\cdot\mathbf{v}$, where ω_o is the apparent frequency measured by an observer on the ground, $\mathbf{k_h} = (k_x, k_y)$ and $\mathbf{v} = (u,v)$ are the horizontal wavenumber and wind vectors with components oriented in the zonal and meridional directions, respectively.

We then estimate λ_z of the events by applying the simplified gravity wave dispersion relation

$$m^2 = \frac{(N^2 - \omega^2)}{(\omega^2 - f^2)} k_h^2,$$

where $m = 2\pi/\lambda_z$ is the vertical wavenumber, N is the Brunt-Väisälä frequency, and f the inertial frequency. We have omitted the term $1/4H^2$ in m^2 equation as it causes only 5% difference on the derived λ_z.

Finally, we derive F_M for large scale waves seen in keograms by evaluating Eq. 12 and Eq. 13 of Vargas et al. (2007) in a similar fashion as shown in Appendix B, although the keogram spectral analysis is noniterative.

Author contributions. FV devised the data processing methods, carried out data analysis. JLC conceived SIMONe and ran the campaign. HCA provided preprocessed meteor radar wind data. MG provided lidar data and revised the manuscript. All authors contribute writing different parts of the manuscript.

Competing interests. None

Acknowledgements. This work was partially supported by the Deutsche Forschungsgemeinschaft (DFG, German Research Foundation) under SPP 1788 (DynamicEarth)-CH1482/2-1. Fabio Vargas' research received external funding from the National Science Foundation under NSF AGS grant 17-59573 and NSF AGS grant 19-03336. Multistatic specular meteor radar winds used in this study can be downloaded from https://databank.illinois.edu/datasets/IDB-8585682. We also want to acknowledge here the SABER team for making available the data used in this publication at http://saber.gats-inc.com/browse_data.php# .

References

Becker, E. and Vadas, S. L.: Secondary Gravity Waves in the Winter Mesosphere: Results From a High-Resolution Global Circulation Model, Journal of Geophysical Research: Atmospheres, 123, 2605–2627, 2018.

Bossert, K., Fritts, D. C., Pautet, P.-D., Williams, B. P., Taylor, M. J., Kaifler, B., Dörnbrack, A., Reid, I. M., Murphy, D. J., Spargo, A. J., and MacKinnon, A. D.: Momentum flux estimates accompanying multiscale gravity waves over Mount Cook, New Zealand, on 13 July 2014 during the DEEPWAVE campaign, Journal of Geophysical Research: Atmospheres, 120, 9323–9337, https://doi.org/https://doi.org/10.1002/2015JD023197, https://agupubs.onlinelibrary.wiley.com/doi/abs/10.1002/2015JD023197, 2015.

Cao, B. and Liu, A. Z.: Intermittency of gravity wave momentum flux in the mesopause region observed with an all-sky airglow imager, Journal of Geophysical Research: Atmospheres, 121, 650–663, https://doi.org/https://doi.org/10.1002/2015JD023802, https://agupubs.onlinelibrary.wiley.com/doi/abs/10.1002/2015JD023802, 2016.

Charuvil, A. H., Chau, J. L., Marino, R., Vierinen, J., Vargas, F., Urco, J. M., Clahsen, M., and Jacobi, C.: Study of second-order wind statistics in the mesosphere and lower thermosphere region from multistatic specular meteor radar observations during the SIMONe 2018 campaign, Atmospheric Chemistry and Physics Discussions, 2020, 1–27, https://doi.org/10.5194/acp-2020-974, https://acp.copernicus.org/preprints/acp-2020-974/, 2020.

Chau, J. L., Stober, G., Hall, C. M., Tsutsumi, M., Laskar, F. I., and Hoffmann, P.: Polar mesospheric horizontal divergence and relative vorticity measurements using multiple specular meteor radars, Radio Science, 52, 811–828, https://doi.org/10.1002/2016RS006225, http://dx.doi.org/10.1002/2016RS006225, 2017.

Chau, J. L., Urco, J. M., Vierinen, J. P., Volz, R. A., Clahsen, M., Pfeffer, N., and Trautner, J.: Novel specular meteor radar systems using coherent MIMO techniques to study the mesosphere and lower thermosphere, Atmospheric Measurement Techniques, 12, 2113–2127, 2019.

Chen, C., Chu, X., McDonald, A. J., Vadas, S. L., Yu, Z., Fong, W., and Lu, X.: Inertia-gravity waves in Antarctica: A case study using simultaneous lidar and radar measurements at McMurdo/Scott Base (77.8 °S, 166.7 °E), Journal of Geophysical Research: Atmospheres, 118, 2794–2808, 2013.

Chen, C., Chu, X., Zhao, J., Roberts, B. R., Yu, Z., Fong, W., Lu, X., and Smith, J. A.: Lidar observations of persistent gravity waves with periods of 3–10 h in the Antarctic middle and upper atmosphere at McMurdo (77.83 °S, 166.67 °E), Journal of Geophysical Research: Space Physics, 121, 1483–1502, 2016.

Ern, M., Preusse, P., Gille, J. C., Hepplewhite, C. L., Mlynczak, M. G., Russell III, J. M., and Riese, M.: Implications for atmospheric dynamics derived from global observations of gravity wave momentum flux in stratosphere and mesosphere, Journal of Geophysical Research: Atmospheres, 116, https://doi.org/https://doi.org/10.1029/2011JD015821, https://agupubs.onlinelibrary.wiley.com/doi/abs/10.1029/2011JD015821, 2011.

Fritts, D. C. and Alexander, M. J.: Gravity wave dynamics and effects in the middle atmosphere, Reviews of Geophysics, 41, 2003.

Fritts, D. C., Vadas, S. L., Wan, K., and Werne, J. A.: Mean and variable forcing of the middle atmosphere by gravity waves, Journal of Atmospheric and Solar-Terrestrial Physics, 68, 247 – 265, 2006.

Garcia, F. J., Taylor, M. J., and Kelley, M. C.: Two-dimensional spectral analysis of mesospheric airglow image data, Appl. Opt., 36, 7374–7385, 1997.

Gobbi, D., Takahashi, H., Clemesha, B., and Batista, P.: Equatorial atomic oxygen profiles derived from rocket observations of OI 557.7 nm airglow emission, Planetary and Space Science, 40, 775 – 781, 1992.

Gong, S., Yang, G., Xu, J., Liu, X., and Li, Q.: Gravity Wave Propagation from the Stratosphere into the Mesosphere Studied with Lidar, Meteor Radar, and TIMED/SABER, Atmosphere, 10, 2019.

Greer, R., Murtagh, D., McDade, I., Dickinson, P., Thomas, L., Jenkins, D., Stegman, J., Llewellyn, E., Witt, G., Mackinnon, D., and Williams, E.: ETON 1: A data base pertinent to the study of energy transfer in the oxygen nightglow, Planetary and Space Science, 34, 771 – 788, 1986.

Heale, C. J., Bossert, K., Vadas, S. L., Hoffmann, L., Dörnbrack, A., Stober, G., Snively, J. B., and Jacobi, C.: Secondary Gravity Waves Generated by Breaking Mountain Waves Over Europe, Journal of Geophysical Research: Atmospheres, 125, e2019JD031 662, 2020.

Holton, J. R.: The generation of mesospheric planetary waves by zonally asymmetric gravity wave breaking, J.atmos., 41, 3427–3430, 1984.

Houghton, J. T.: The stratosphere and mesosphere, Quarterly Journal of the Royal Meteorological Society, 104, 1–29, 1978.

Li, Z.: An observational investigation on gravity wave characteristics and propagation in the lower stratosphere and mesopause, Ph.D. thesis, University of Illinois at Urbana-Champaign, 2011.

Li, Z., Liu, A. Z., Lu, X., Swenson, G. R., and Franke, S. J.: Gravity wave characteristics from OH airglow imager over Maui, Journal of Geophysical Research: Atmospheres, 116, 2011.

Melo, S., Takahashi, H., Clemesha, B., Batista, P., and Simonich, D.: Atomic oxygen concentrations from rocket airglow observations in the equatorial region, Journal of Atmospheric and Terrestrial Physics, 58, 1935–1942, 1996.

Mlynczak, M. G.: Energetics of the mesosphere and lower thermosphere and the SABER experiment, Advances in Space Research, 20, 1177 – 1183, https://doi.org/https://doi.org/10.1016/S0273-1177(97)00769-2, http://www.sciencedirect.com/science/article/pii/S0273117797007692, coupling and Energetics in the Stratosphere-Mesosphere-Thermosphere- Ionosphere System, 1997.

Reichert, R., Kaifler, B., Kaifler, N., Rapp, M., Pautet, P.-D., Taylor, M. J., Kozlovsky, A., Lester, M., and Kivi, R.: Retrieval of intrinsic mesospheric gravity wave parameters using lidar and airglow temperature and meteor radar wind data, Atmospheric Measurement Techniques, 12, 5997–6015, https://doi.org/10.5194/amt-12-5997-2019, https://amt.copernicus.org/articles/12/5997/2019/, 2019.

Russell, J., Mlynczak, M., Gordley, L., Tansock, J., and Esplin, R.: Overview of the SABER experiment and preliminary calibration results, Proceedings of SPIE - The International Society for Optical Engineering, 3756, 277–288, 1999.

Sato, K., Kohma, M., Tsutsumi, M., and Sato, T.: Frequency spectra and vertical profiles of wind fluctuations in the summer Antarctic mesosphere revealed by MST radar observations, Journal of Geophysical Research: Atmospheres, 122, 3–19, https://doi.org/https://doi.org/10.1002/2016JD025834, https://agupubs.onlinelibrary.wiley.com/doi/abs/10.1002/2016JD025834, 2017.

Smith, S. M., Setvák, M., Beletsky, Y., Baumgardner, J., and Mendillo, M.: Mesospheric Gravity Wave Momentum Flux Associated With a Large Thunderstorm Complex, Journal of Geophysical Research: Atmospheres, 125, e2020JD033 381, 2020.

Solomon, S., R., G. R., Edgeworth, M. M., Adrian, P. J., L., T., and Robert, W.: Current understanding of mesospheric transport processes, Philosophical Transactions of the Royal Society of London. Series A, Mathematical and Physical Sciences, pp. 655–666, 1987.

Stober, G. and Chau, J. L.: A multistatic and multifrequency novel approach for specular meteor radars to improve wind measurements in the MLT region, Radio Science, 50, 431–442, https://doi.org/10.1002/2014RS005591, http://doi.wiley.com/10.1002/2014RS005591, 2015.

Suzuki, S., Nakamura, T., Ejiri, M. K., Tsutsumi, M., Shiokawa, K., and Kawahara, T. D.: Simultaneous airglow, lidar, and radar measurements of mesospheric gravity waves over Japan, Journal of Geophysical Research: Atmospheres, 115, https://doi.org/https://doi.org/10.1029/2010JD014674, https://agupubs.onlinelibrary.wiley.com/doi/abs/10.1029/2010JD014674, 2010.

Swenson, G. R. and Espy, P. J.: Observations of 2-dimensional airglow structure and Na density from the ALOHA, October 9, 1993 ‘storm flight’, Geophysical Research Letters, 22, 2845–2848, 1995.

Swenson, G. R. and Mende, S. B.: OH emission and gravity waves (including a breaking wave) in all-sky imagery from Bear Lake, UT, Geophysical Research Letters, 21, 2239–2242, https://doi.org/https://doi.org/10.1029/94GL02112, https://agupubs.onlinelibrary.wiley.com/doi/abs/10.1029/94GL02112, 1994.

Tang, J., Kamalabadi, F., Franke, S. J., Liu, A. Z., and Swenson, G. R.: Estimation of gravity wave momentum flux with spectroscopic imaging, IEEE Transactions on Geoscience and Remote Sensing, 43, 103–109, 2005.

Urco, J. M., Chau, J. L., Milla, M. A., Vierinen, J. P., and Weber, T.: Coherent MIMO to improve aperture synthesis radar imaging of field-aligned irregularities: First results at Jicamarca, IEEE Transactions on Geoscience and Remote Sensing, 56, 2980–2990, https://doi.org/10.1109/TGRS.2017.2788425, 2018.

Urco, J. M., Chau, J. L., Weber, T., Vierinen, J., and Volz, R.: Sparse signal recovery in MIMO specular meteorradars with waveform diversity, IEEE Trans. Geosci. Remote Sensing, p. 1, papers2://publication/uuid/3BE7DFC6-C58D-4567-AB89-92B77BC87721, 2019.

Vadas, S. L. and Becker, E.: Numerical Modeling of the Excitation, Propagation, and Dissipation of Primary and Secondary Gravity Waves during Wintertime at McMurdo Station in the Antarctic, Journal of Geophysical Research: Atmospheres, 123, 9326–9369, 2018.

Vadas, S. L., Zhao, J., Chu, X., and Becker, E.: The Excitation of Secondary Gravity Waves From Local Body Forces: Theory and Observation, Journal of Geophysical Research: Atmospheres, 123, 9296–9325, 2018.

Vargas, F.: Uncertainties in gravity wave parameters, momentum fluxes, and flux divergences estimated from multi-layer measurements of mesospheric nightglow layers, Advances in Space Research, 63, 967 – 985, 2019.

Vargas, F., Swenson, G., Liu, A., and Gobbi, D.: O(1S), OH, and O2(b) airglow layer perturbations due to AGWs and their implied effects on the atmosphere, Journal of Geophysical Research: Atmospheres, 112, 2007.

Vargas, F., Gobbi, D., Takahashi, H., and Lima, L. M.: Gravity wave amplitudes and momentum fluxes inferred from OH airglow intensities and meteor radar winds during SpreadFEx, Annales Geophysicae, 27, 2361–2369, 2009.

Vargas, F., Swenson, G., and Liu, A.: Evidence of high frequency gravity wave forcing on the meridional residual circulation at the mesopause region, Advances in Space Research, 56, 1844 – 1853, 2015.

Vargas, F., Swenson, G., Liu, A., and Pautet, D.: Evidence of the excitation of a ring-like gravity wave in the mesosphere over the Andes Lidar Observatory, Journal of Geophysical Research: Atmospheres, 121, 8896–8912, 2016.

Vargas, F., Yang, G., Batista, P., and Gobbi, D.: Growth Rate of Gravity Wave Amplitudes Observed in Sodium Lidar Density Profiles and Nightglow Image Data, Atmosphere, 10, 2019.

Vargas, F., Brum, C., Terra, P., and Gobbi, D.: Mean Zonal Drift Velocities of Plasma Bubbles Estimated from Keograms of Nightglow All-Sky Images from the Brazilian Sector, Atmosphere, 11, 2020.

Vierinen, J., Chau, J. L., Pfeffer, N., Clahsen, M., and Stober, G.: Coded continuous wave meteor radar, Atmospheric Measurement Techniques, 9, 829–839, https://doi.org/10.5194/amt-9-829-2016, https://www.atmos-meas-tech.net/9/829/2016/, 2016.

Vierinen, J., Chau, J. L., Charuvil, H., Urco, J. M., Clahsen, M., Avsarkisov, V., Marino, R., and Volz, R.: Observing Mesospheric Turbulence With Specular Meteor Radars: A Novel Method for Estimating Second-Order Statistics of Wind Velocity, Earth and Space Science, 6, 1171–1195, 2019.

Vincent, R. A.: Gravity-wave motions in the mesosphere, Journal of Atmospheric and Terrestrial Physics, 46, 119–128, 1984.

Vincent, R. A. and Alexander, M. J.: Balloon-borne observations of short vertical wavelength gravity waves and interaction with QBO winds, Journal of Geophysical Research: Atmospheres, n/a, e2020JD032 779, 2020.

Vincent, R. A. and Fritts, D. C.: A Climatology of Gravity Wave Motions in the Mesopause Region at Adelaide, Australia., Journal of Atmospheric Sciences, 44, 748–760, 1987.

Wüst, S., Bittner, M., Yee, J.-H., Mlynczak, M. G., and Russell III, J. M.: Variability of the Brunt–Väisälä frequency at the OH* layer height, Atmospheric Measurement Techniques, 10, 4895–4903, https://doi.org/10.5194/amt-10-4895-2017, https://amt.copernicus.org/articles/10/4895/2017/, 2017.

Yuan, L. and Fritts, D. C.: Influence of a mean shear on the dynamical instability of an inertio-gravity wave, Journal of Atmospheric Sciences, 46, 2562–2568, 1989.

Table 1. Configuration of the All-sky imager system used to collect airglow images during the SIMONe–2018 Campaign. Airglow images of the campaign are available at http://sirius.bu.edu/data/.

Filter	Emission	Wavelength (nm)	Integration Time (sec)
RG695	OH	695.0–1050.0	15
6050C	Background OH	605.0	120
5893C	NaD	589.3	120
8660C	$O_2(0,1)$	864.5	120
5577C	$O(^1S)$	557.7	120
6300C	$O(^1D)$	630.0	120

Table 2. Centroid, peak, and FWHM of the OH, O_2, and $O(^1S)$ layers measured and calculated using TIMED/SABER data collected near Kühlungsborn during SIMONe–2018 campaign.

Emission	Wavelength	Origin	Layer Centroid (km)	Layer Peak (km)	FWHM (km)
OH(A)	2.1 μm	SABER	$\sim$87.3	$\sim$86.4	$\sim$14.3
OH(B)	1.6 μm	SABER	$\sim$85.8	$\sim$84.8	$\sim$12.5
OH(8,3)	727.3 nm	simulation	$\sim$89.4	$\sim$86.5	$\sim$18.7
O_2(0-1)	864.5 nm	simulation	$\sim$91.1	$\sim$88.0	$\sim$14.6
$O(^1S)$	557.7 nm	simulation	$\sim$93.3	$\sim$91.4	$\sim$16.7

Table 3. Estimated features of the large-scale waves observed in the airglow and meteor radar wind data.

Date	λ_h (km)	λ_z (km)	τ_o (h)	τ_i (h)	c_o ($\mathrm{ms^{-1}}$)	c_i ($\mathrm{ms^{-1}}$)	I' (%)	T' (%)	F_M ($\mathrm{m^2s^{-2}}$)
Nov. 3–4	1365±136 (Fig.09)	25.1±2.5 (Fig.09) 25.6±1.0 (Fig.10)	4.0±1.0 (Fig.08) 4.6±1.0 (Fig.09) 4.3±1.0 (Fig.10)	4.7	81.6	80.3	36.5±3.6	9.1	21.2±8.4
Nov. 6–7	4096±409 (Fig.09)	20.5±2.0 (Fig.9) 21.3±1.0 (Fig.10)	8.0±1.0 (Fig.08) 9.1±1.0 (Fig.09) 8.0±1.0 (Fig.10)	11.5	125.2	99.1	47.9±4.8	13.7	29.6±11.8

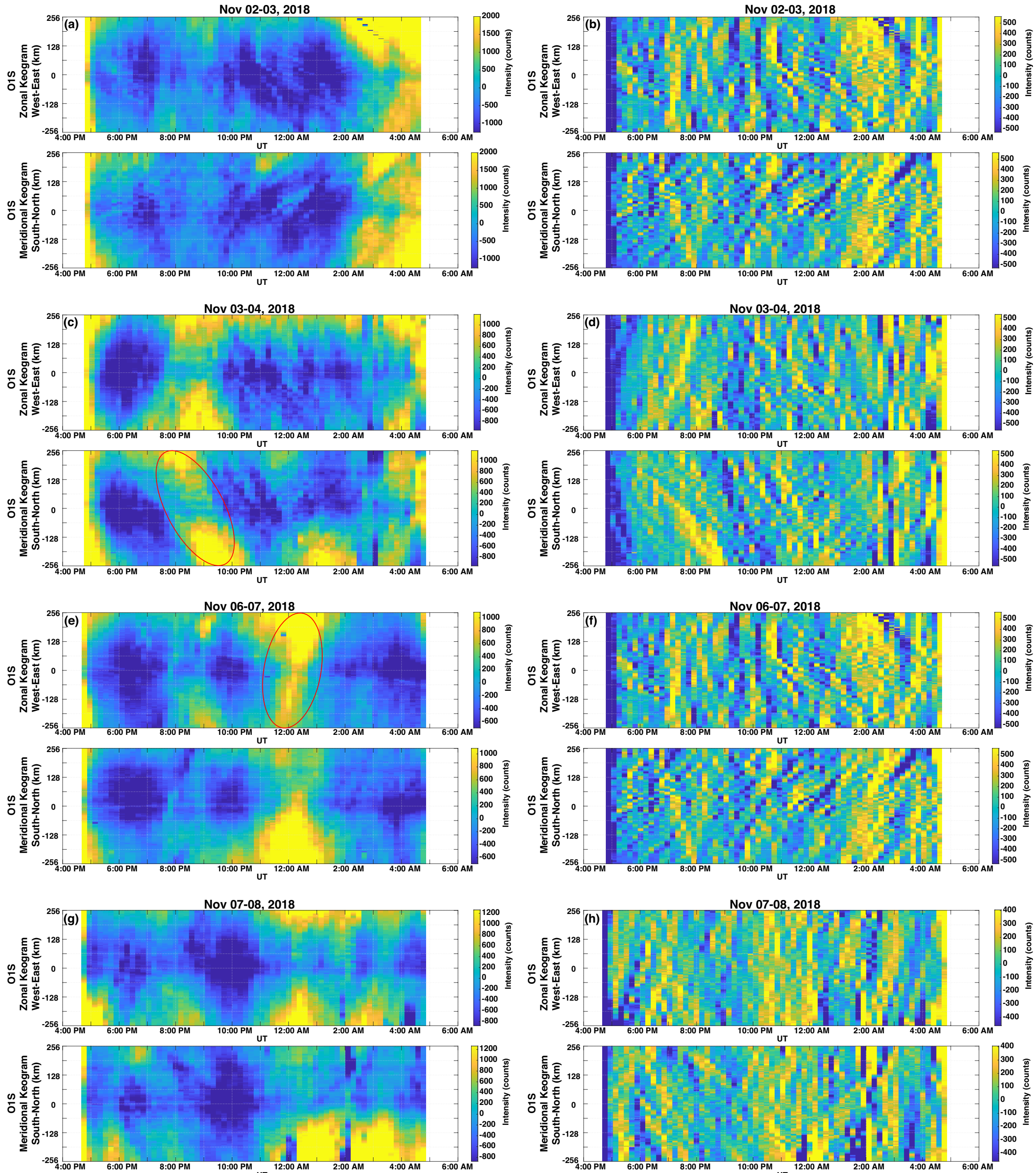

Figure 1. Composite keograms of O(^{1}S) airglow images taken on clear nights during the SIMONe–2018 campaign. The keograms in panels (a), (c), (e), and (f) were built using light frame images, while keograms in panels (b), (d), (f), and (g) were built using TD images. Time-difference keograms show short-period waves in higher contrast, while light frame keograms show mainly long-period oscillations. Note the enhanced airglow brightness (red ellipses) on Nov. 3–4 (meridional keogram) and Nov. 6–7 (zonal keogram) associated with large-scale gravity waves also seen in wind fluctuations of Figure 2.

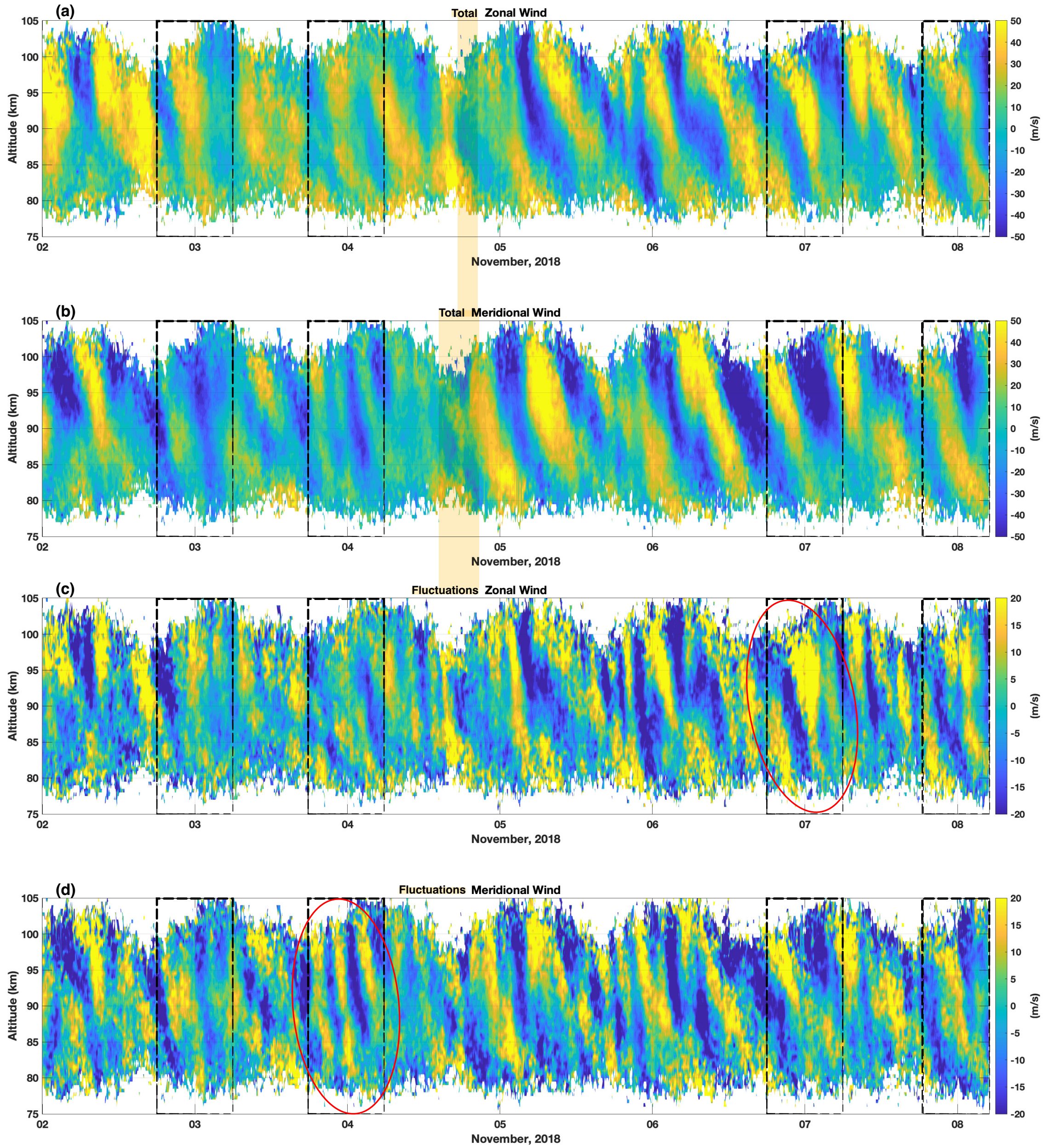

Figure 2. (a) Zonal and (b) meridional wind measurements for the duration of the SIMONe–2018 campaign generated by the MSMR network. Note the dominance of the semidiurnal tide on the horizontal wind. (c) Zonal and (d) and meridional wind fluctuations of $\tau_o \leq 4$ hours. Note the presence of coherent gravity wave features (red ellipses) on Nov. 3–4 in the meridional wind fluctuations and on Nov. 6–7 in the zonal wind fluctuations coincident with enhanced keogram brightness for the same nights in Figure 1. Dashed boxes indicate hours of simultaneous operation of the ASI and MSMR systems.

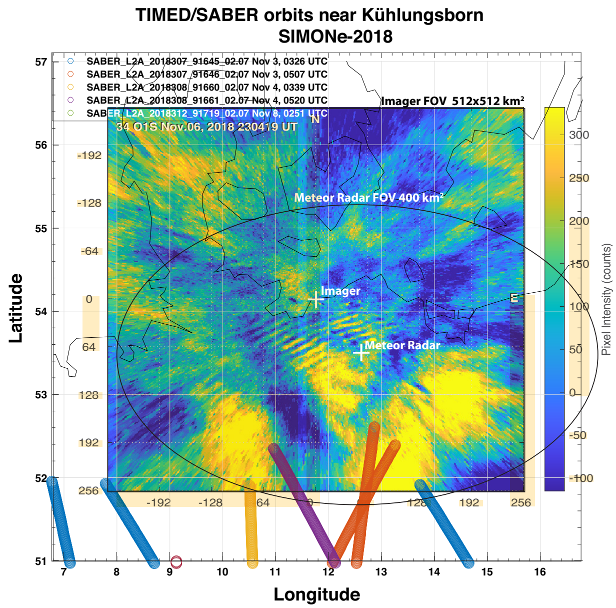

Figure 3. Individual TIMED/SABER satellite orbits near Kühlungsborn during the SIMONe–2018 campaign. The colored lines represent the location where vertical atmospheric profiles were measure, not the actual satellite locus. The day and time of each orbit is indicated in the legend. The field of view of 512x512 km^2 of the airglow camera projected at $\sim$ 95 km is indicated by the O(^{1}S), TD image mapped onto geographic coordinates, while the ellipse indicates the field of view of the MSMR system. The white crosses indicates the coordinates of the imager system in the Kühlungsborn observatory, and the meteor radar system.

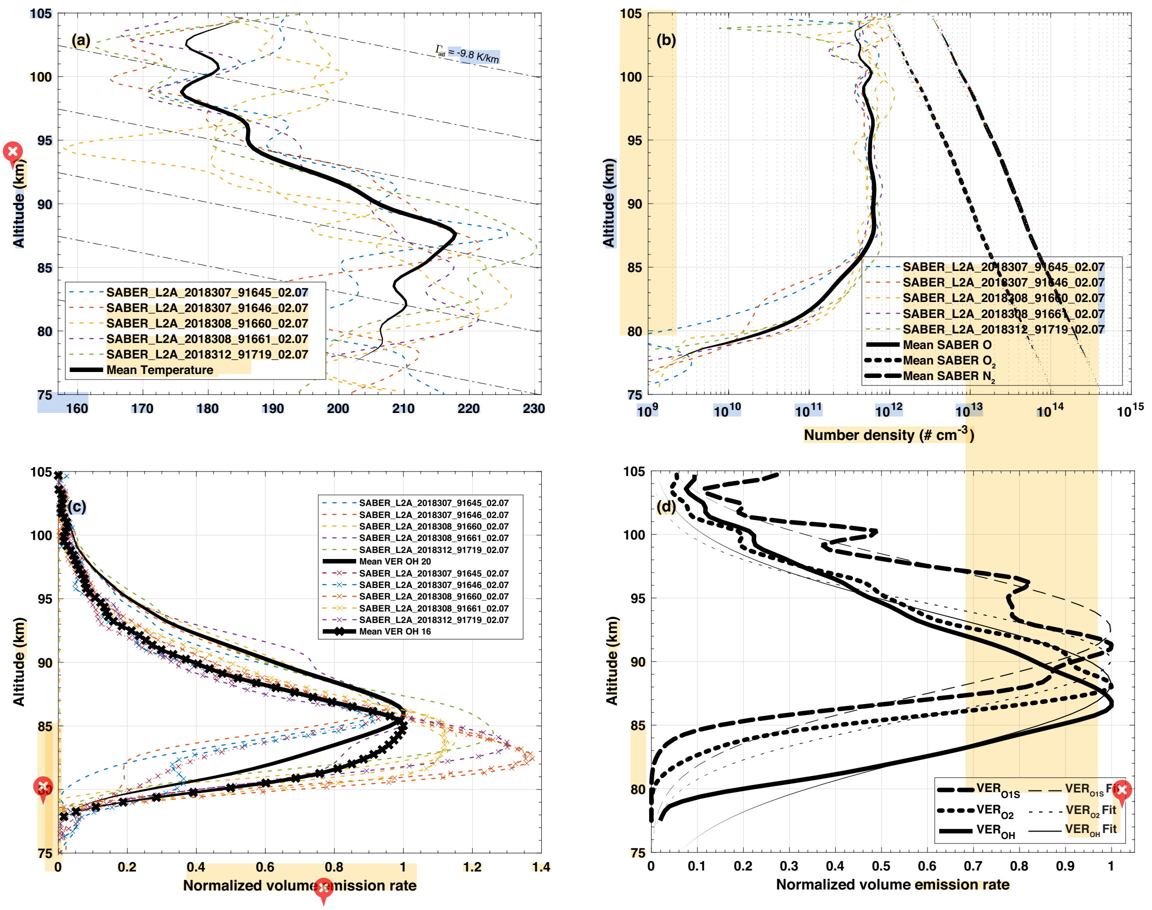

Figure 4. (a) Temperature, (b) atomic oxygen, molecular oxygen, molecular nitrogen number densities, and (c) OH20 (2.1 μm OH(A)) and OH16 (1.6 μm OH(B)) volume emission rates collected by TIMED/SABER satellite near Kühlungsborn during the SIMONe–2018 campaign within four degrees of latitude or longitude of the observatory. (d) Calculated volume emission rates for OH(8,3), O_2(0,1), and $O(^1S)$ layers (thick black lines) using SABER mean profiles in panels (a) and (b). Colored dotted lines in (a), (b), and (c) indicate individual orbits of the satellite, while thick lines indicate the mean of the individual orbits. Gray dash-dot lines in (a) indicate the adiabatic lapse rate Γ_{ad} =-9.8 K/km. Thinner black lines in (d) are Gaussian fits of the calculated VER profiles. Individual VER airglow layer features for both measured and calculated VER are in Table 2. We have used SABER data version 2.07 to compose these plots.

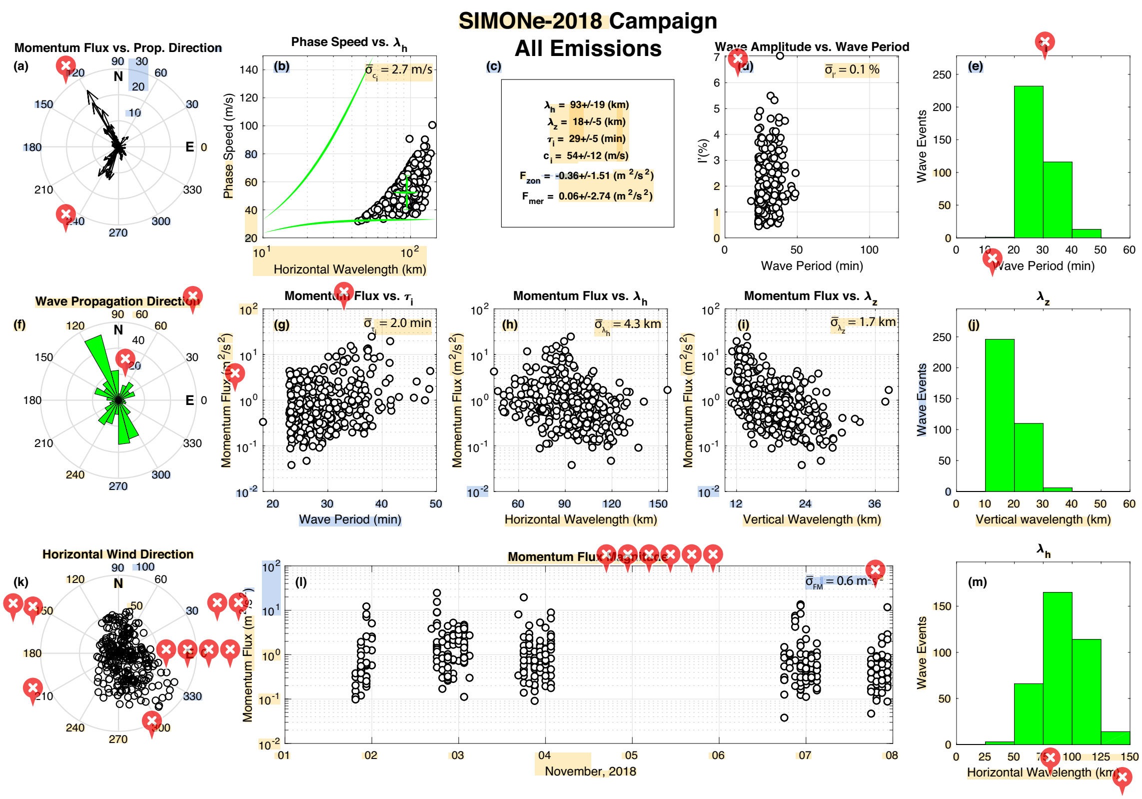

Figure 5. Short-period wave parameters obtained from OH, O_2, $O(^1S)$, and Na airglow image analysis using the auto-detection method (Tang et al., 2005; Vargas et al., 2009; Vargas, 2019). The mean measurement error is indicated in the chart of each wave parameter. Plots of waves detected in each emission separately are in the supplementary files of this paper.

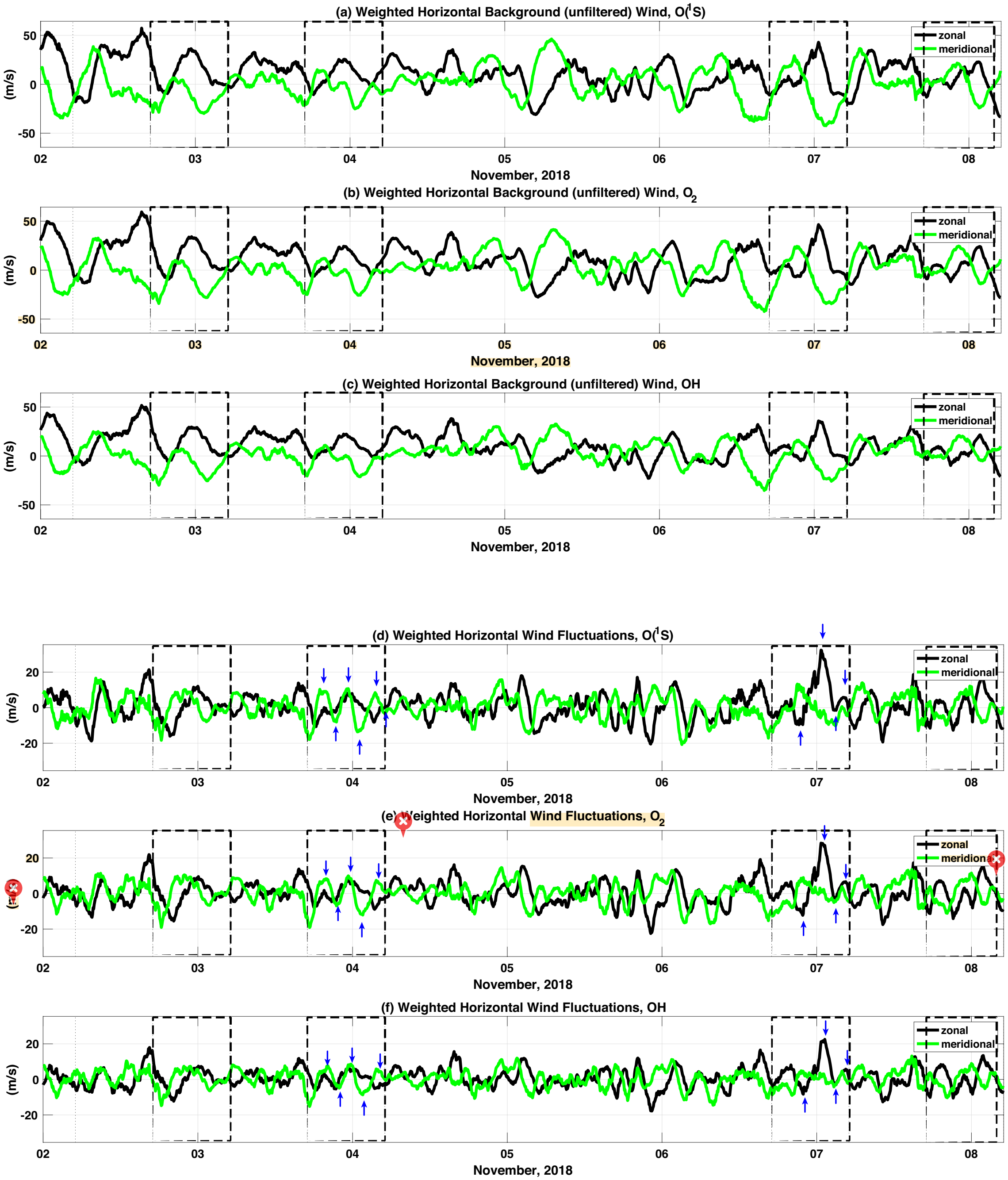

Figure 6. (a) O(^{1}S), (b) O_2, and (c) OH volume emission rate weighted zonal and meridional background (unfiltered) winds. (d) O(^{1}S), (e) O_2, and (f) OH volume emission rate weighted zonal and meridional wind fluctuations. Wind fluctuations were obtained first by averaging the wind over 400 km^2 field of view using a 4-hour temporal, 4-km vertical windows to obtain winds representing large-scales variations, then subtracting these estimates from the background wind field. The vertical blue arrows indicate coherent wind fluctuations also seen in the airglow brightness. Dashed boxes indicate hours of simultaneous operation of the ASI and MSMR system.

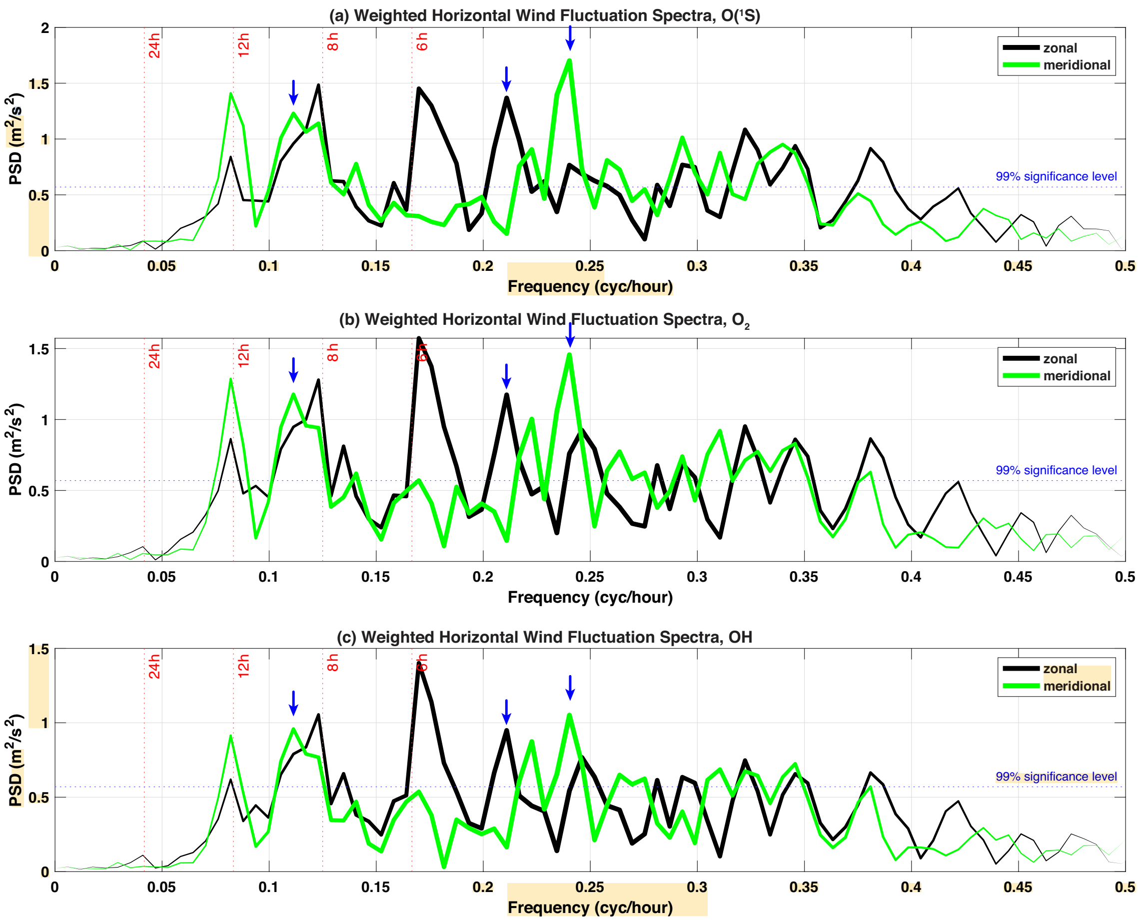

Figure 7. Spectra of weighted zonal and meridional wind fluctuation of Fig. 6. The dashed red lines indicate tidal periods. The vertical blue arrows indicate wave frequencies of persisting wave structures also seen in the airglow brightness. Statistical 99% significance level is indicated by dotted blue lines.

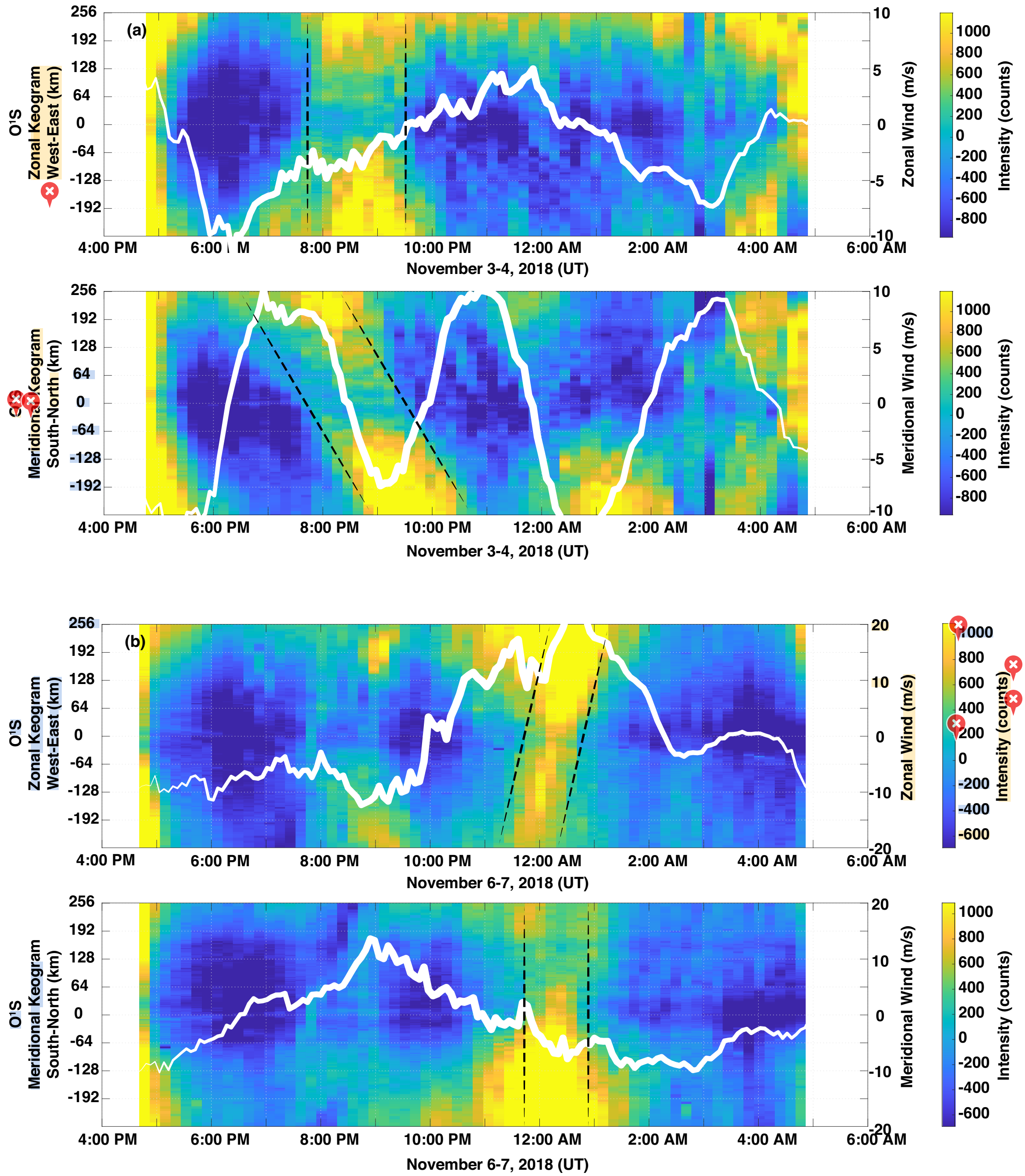

Figure 8. Enhanced contrast keograms of O(^{1}S) airglow for (a) Nov. 3–4 and (b) Nov. 6–7, 2018. The keogram of Nov. 3–4 shows a large amplitude, large-scale gravity wave at 2000-2200 UTC heading south. A large-scale wave is also seen on Nov. 6–7 propagating eastward at 0000 UTC. The white continuous lines on the keograms indicate the wind fluctuations weighted by the O(^{1}S) volume emission rate.

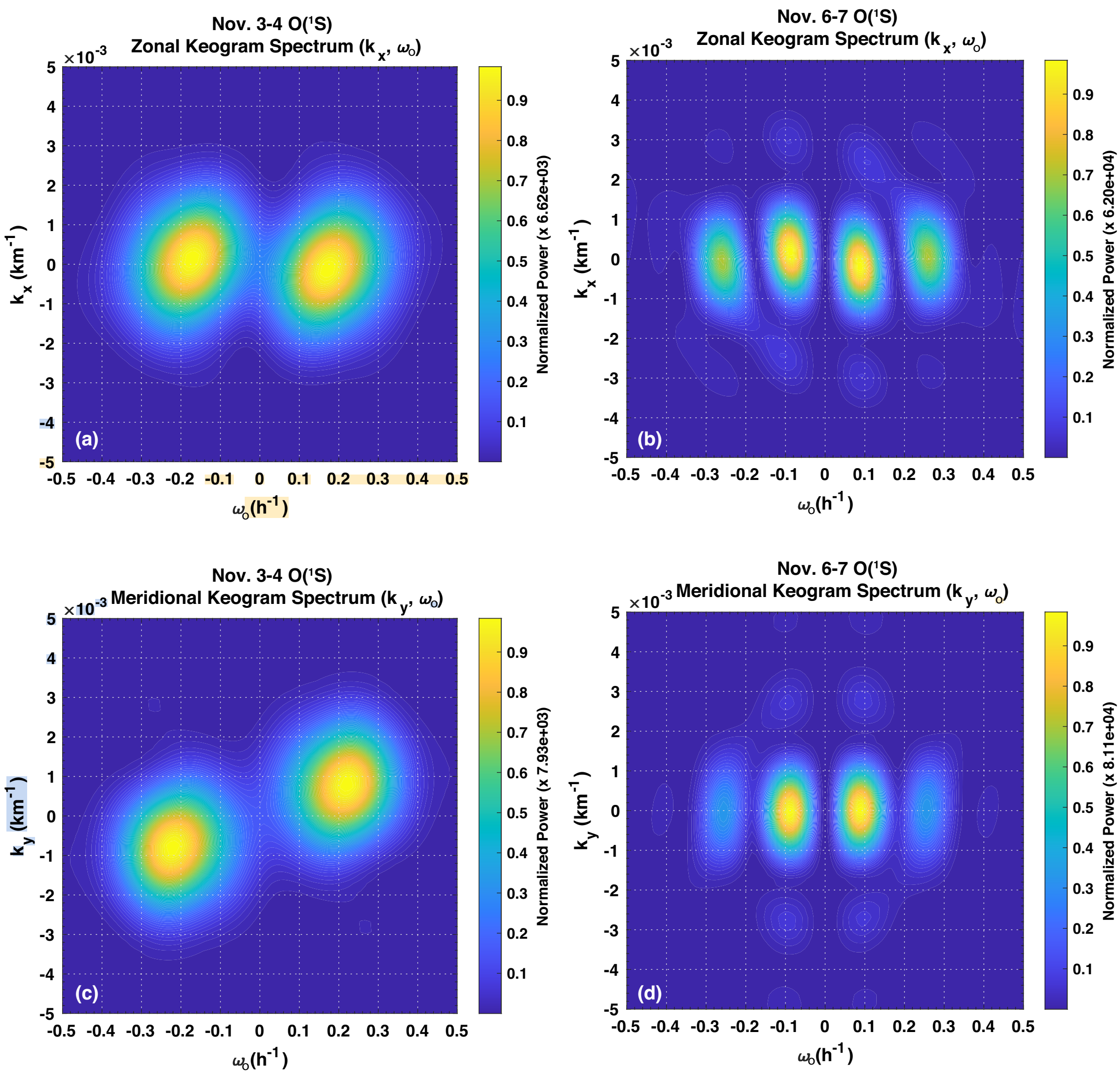

Figure 9. Composite (k_x, ω_o) and (k_y, ω_o) spectra of the keograms in Fig. 8 for the nights of Nov. 3–4 (panels a and c) and Nov. 6–7 (panels b and d).

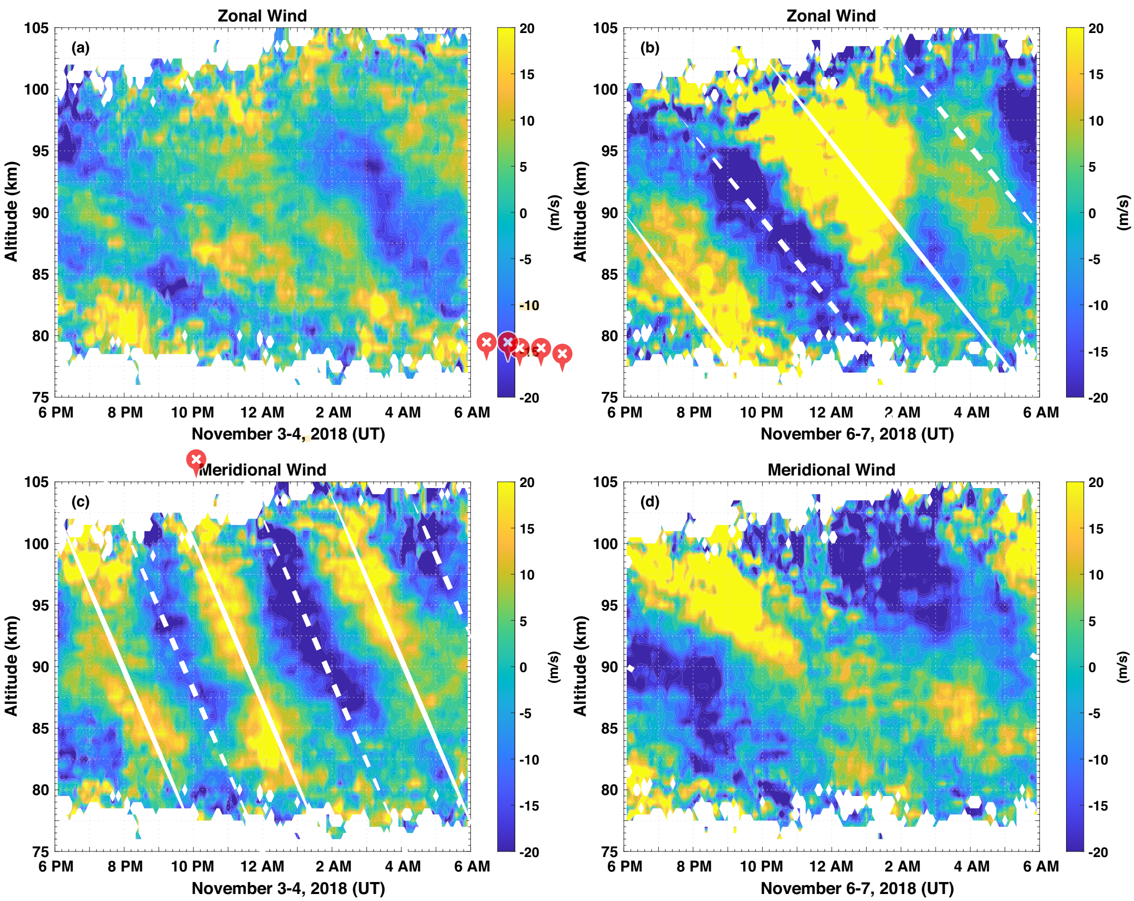

Figure 10. Time-altitude cross section of the zonal and meridional wind fluctuations for the nights of Nov. 3–4 and Nov. 6–7, 2018. The continuous (dashed) white lines indicate crests (troughs) of the oscillations as well as the descending phase (ascending energy propagation) of the waves. Notice the coherent $\tau_o \sim$4.3 hours gravity wave oscillation on Nov. 3–4 with $\lambda_z \sim$25.6 km. The zonal wind oscillation on Nov. 6–7 corresponds to a $\lambda_z \sim$21.3 km, $\tau_o \sim$8.0 hours gravity wave.